# Interaction of synthetic jets with a massively separated three-dimensional flow field

Nicholas Rathay [*] and Michael Amitay [†]
*Mechanical, Aerospace, and Nuclear Engineering Department, Rensselaer Polytechnic Institute, Troy, New York 12180, USA*

(Received 28 November 2021; accepted 7 March 2022; published 24 March 2022)

The interaction of an array of finite span synthetic jet actuators with a massively separated flow was explored experimentally over a cantilevered, swept, and tapered model having a deflected control surface. The synthetic jet actuators were placed slightly upstream of the control surface hinge-line of the wind tunnel model. The flow physics associated with the interaction of multiple jets and the separated crossflow over the control surface was investigated using stereoscopic particle image velocimetry. Experiments were conducted at two spanwise regions along the model, where separation severity varied. At the outboard region, the baseline flow field was characterized by a severe separation that was quasiuniform in the spanwise direction. At the inboard measurement domain, separation was milder but increased in severity in the outboard direction. When a single jet was activated, separation was reduced downstream and outboard of the jet orifice. In addition, spanwise velocity was augmented outboard of the jet's structures at the outboard measurement domain from an oblique vortex that was observed at the spanwise location where separation severity increased (as the flow approached the baseline state). In the inboard region, this vortex was not observed and the spanwise velocity decreased with a single jet active. When more jets were actuated along the span, the overall severity of separation decreased at both locations. Despite this, in the outboard region, the spanwise velocity near the surface was enhanced, and the strength of the jets' vortical structures decreased as more jets were activated (i.e., they negatively impacted one another). On the contrary, at the inboard region, the jets beneficially affected each other. These differences were hypothesized to be related to the oblique vortices that were distinguishable outboard but not inboard with all jets active.

DOI: 10.1103/PhysRevFluids.7.034702

## I. INTRODUCTION

Active flow control has become a widely researched area in the last three decades (Anders *et al.* [1]) as significant advancements in aerodynamic systems cannot be achieved using traditional techniques. There are a large variety of ways in which active flow control can be used to manipulate a flow field. One such branch of active flow control is separation control, where there are an abundance of methods and actuators. All of the actuators come with their own advantages and disadvantages (Cattafesta and Sheplak [2]). Synthetic jet actuators are one type that has many advantages, such as their low power consumption, weight, and mechanical simplicity. Therefore, synthetic jets have been heavily studied, and there is a great deal known about them. However, there is still much to learn.

[*]Currently at General Electric Research Center.
[†]amitam@rpi.edu

 

Synthetic jets are zero-net mass flux devices that are formed by the time periodic motion of a diaphragm (Smith and Glezer [3], and Glezer and Amitay [4]). Smith and Glezer [3] conducted one of the first experimental synthetic jet studies with a rectangular jet that had an aspect ratio (orifice length/width) of 150. They showed a train of discrete vortices near the jet orifice that advect downstream, lose their coherence, and coalesce into a turbulent jet. Since the jet is formed from the working fluid, it is zero-net mass flux, and hence requires no external air supply (and associated complexity). In comparison to a steady jet, synthetic jets entrain more fluid, and therefore grow more rapidly (Smith and Swift [5] and Van Buren and Amitay [6]).

Amitay and Cannelle [7] investigated the streamwise and spanwise evolution of a finite span synthetic jet and explored the formation of vortical structures at three orifice aspect ratios (50.8, 76.2, and 101.6) in quiescent conditions. They observed a two-dimensional (2D) flow near the orifice. Farther downstream though, the finite nature of the jet resulted in the development of secondary, counter-rotating vortical structures, where their strength and wavelength varied with the aspect ratio and the stroke length. In addition, there has been a significant amount of other work conducted with synthetic jets in quiescent conditions that have both rectangular (Yao *et al.* [8], Kotapati *et al.* [9], Van Buren *et al.* [10,11]) and circular orifices (Crook and Wood [12], Zhong *et al.* [13], Wu and Leschziner [14]).

There has also been research focused on the interaction of synthetic jets with a boundary layer over a flat plate. Numerical simulations of a 2D synthetic jet showed that the presence of a crossflow resulted in different dynamics of the jet's vortices (Mittal *et al.* [15]). Van Buren *et al.* [16] investigated experimentally the formation and evolution of flow structures due to the interaction of low aspect ratio, rectangular, finite-span synthetic jets with a zero-pressure gradient laminar boundary layer. They showed that the interaction was found to be associated with two sets of flow structures: (1) an unsteady recirculation region immediately downstream of the orifice due to virtual blockage, and (2) a quasisteady streamwise vortex pair farther downstream. Moreover, the interaction of a boundary layer and multiple synthetic jets with rectangular and circular orifices was investigated by Smith [17] and Watson *et al.* [18], respectively. Although this is the subject of some debate, there is evidence that slot (rectangular) jets have a greater effectiveness than circular jets (Leschziner and Lardeau [19]), and therefore, they were selected for the present work.

The majority of the work with synthetic jets in a 2D crossflow has been conducted with airfoils. McCormick [20] used synthetic jets actuated at a dimensionless frequency of $O(1)$ to control leading edge separation over a 2D airfoil. The jets were placed upstream of the separation location and were inclined at approximately 20° with respect to the surface. Separation control at frequency of $O(1)$ can induce unsteady flow reattachment though (Amitay and Glezer [21]). To avoid this, synthetic jets can also be operated at a dimensionless frequency of $O(10)$, which decouples the jet driving frequency from the shedding frequency (Glezer and Amitay [4] and Amitay and Glezer [21]). This technique was first demonstrated for separation control on a 2D, 24% thick airfoil section with a cylindrical leading edge (Amitay *et al.* [22]). Without flow control, the airfoil stalled at an angle of attack of 5 °, and with synthetic-jet-based flow control, the flow was completely attached up to 15°. Also, the most efficient location for control was found to be as close to the separation as possible. More recently, DeSalvo *et al.* [23] conducted experiments with synthetic jets on a 2D airfoil with a single-element flap. It was found that better performance with finite span jets could be obtained at a lower global $C_\mu$ by using fewer, higher powered individual actuators.

In addition to 2D airfoils, there has also been work conducted on 3D configurations to a more limited extent. Greenblatt and Washburn [24] compared the effectiveness of synthetic jets actuated at $O(1)$ on the flap shoulder of unswept and sweptback semi-span wing wind tunnel models. The effect of control on the unswept model did not significantly differ from that of an equivalent 2D model; it was nearly uniform across the span. With the swept model though, the jets were able to create a large change inboard, but this effect degraded outboard. Furthermore, simulations of a swept wing configuration were undertaken with continuous and segmented jet orifices, where it was found that the segmented configuration was more effective at controlling separation (Holl *et al.* [25]). This was hypothesized to be related to the longitudinal vortices that were created as a result of the finite nature of the jets.

The interaction of a single finite span synthetic jet and the crossflow over a finite span wing was investigated in a joint numerical and experimental effort by Sahni *et al.* [26]. The authors observed spanwise and edge vortices formed at the orifice edges, where, farther downstream, secondary structures were formed. Elimelech *et al.* [27] conducted similar experiments with a single finite span synthetic jet and a finite span wing swept at 30°. In this case, the jet developed three-dimensionality much closer to the orifice, and it consisted of a superposition of spanwise and edge vortices. This work was then taken one step farther by Vasile and Amitay [28], where the same wind tunnel model was used to explore the interaction of an array of three synthetic jets (placed along the span) with the crossflow. The jets, spaced 43 orifice widths apart, did not appear to have a noticeable influence on one another.

Prior to the present study, the flow physics associated with the interaction of finite span synthetic jets and a crossflow that was attached or mildly separated was fairly well understood. However, the understanding of how an array of synthetic jets interacted with a severely separated crossflow and how the interaction changed based on separated severity was a largely unstudied subject. It was and still is crucial for flow control to gain this knowledge, as synthetic jets will most likely be used in such an application (e.g., Maines *et al.* [29]). This was therefore the motivation behind the present investigation, which was a continuation of both applied and fundamental research.

The applied portion of the work initially focused on determining the general performance enhancement of a vertical tail due to the activation of an array of synthetic jet actuators (Rathay *et al.* [30,31]). It was found that the synthetic jets were capable of increasing the side force coefficient by up 34% on the tail model, and that control effectiveness was highly dependent on the spanwise location of the jets, as well as the flap deflection. Additionally, the influence of multiple synthetic jet parameters was studied. That investigation produced the surprising result where, in specific spanwise locations and for some conditions, side force augmentation was enhanced when jet spacing was larger (i.e., when only a portion of the jets was activated). Furthermore, fundamental research on the interaction of a single synthetic jet, located at mid-span, with severely separated crossflow over the control surface was conducted by Jansen *et al.* [32]. The evolution of the vortex rings that are formed at the jet's finite span orifice was captured, and it was found that the jet enhances the spanwise component of velocity outboard of its location.

The present study takes the next step in this fundamental work, where the sweptback and tapered model having a control surface is simply a means of generating separated flow that varies in severity along the span. A single jet and an array of jets were activated and experimentally investigated at two spanwise regions. The objective is to enhance the understanding of how finite span synthetic jets interact with the separated crossflow and with each other as well as how their interaction depends on separation severity and spanwise uniformity.

## II. EXPERIMENTAL SETUP

Experiments were conducted at Rensselaer Polytechnic Institute in an open-return tunnel with a cross-section of $0.8 \times 0.8$ m and a working length of 5 m. The maximum speed of the tunnel was 50 m/s, and the turbulence levels were less than 0.2%. A swept back, finite span, cantilevered, and tapered model was designed, fabricated, and installed in the tunnel.

The model had a NACA 0012 cross-section, and the tapered planform shape with a leading edge sweep angle $\Lambda_{\mathrm{LE}} = 45^\circ$, taper ratio $\lambda = 0.36$ ($\lambda = c_t/c_r$, where $c_t$ and $c_t$ are the tip and root chords, respectively), semi-span $b/2 = 0.53\,\mathrm{m}$, mean aerodynamic chord of the airfoil $\bar{c} = 0.271\,\mathrm{m}$, and planform area $S = 0.134\,\mathrm{m}^2$ (Fig. 1). The freestream velocity was held constant at $U_\infty = 20\,\mathrm{m/s}$, corresponding to a mean chord-based Reynolds number $\mathrm{Re}_{\bar{c}} = 250\,000$. For the present experiments, the angle of attack of the model was held constant at 0°. The model was also equipped with a control surface that was 29.5% of the mean chord and was deflected to 30°. Additionally, the aforementioned deflection was chosen so that the flow would be mildly separated

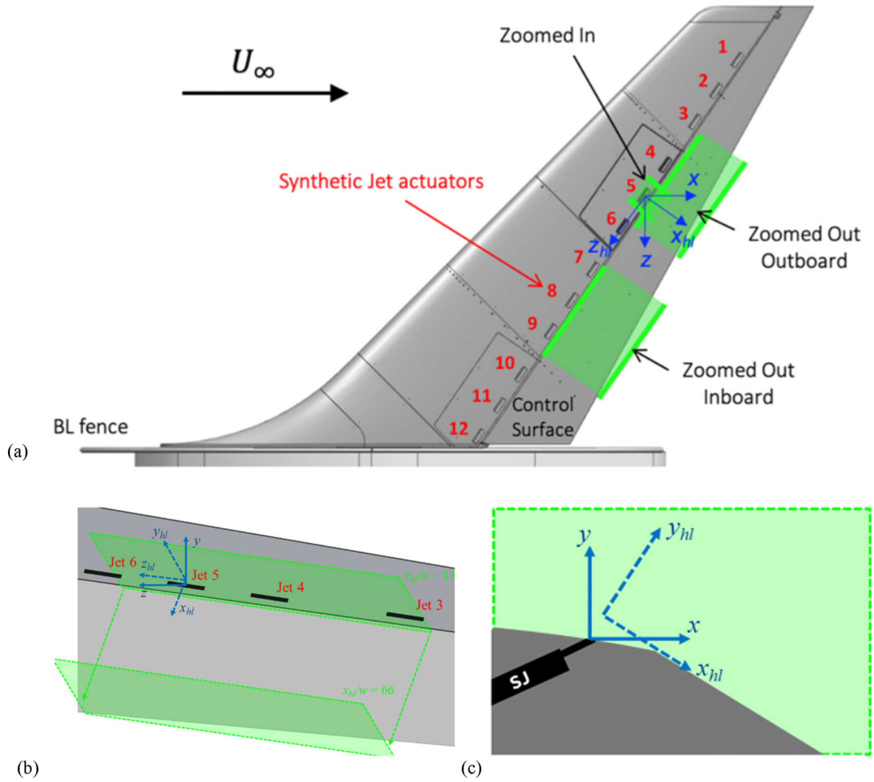


FIG. 1. Diagram of the finite span wind tunnel model showing the regions in which SPIV data were collected in multiple orientations: (a) side view of the entire model, (b) a view from behind the model looking upstream in the $-x$ direction with the green planes signifying the zoomed-out experiments in the outboard region, and (c) a side view with the green planes signifying the zoomed-in experiments.

toward the inboard side of the model and more severely separated outboard (which will be described in more detail later in the paper).

To ensure a turbulent boundary layer, a trip was placed at 5% chord on the suction side of the model and at 10% chord on the pressure side. The trip was composed of 24-grit roughness distributed uniformly on a double stick tape. The size of the grit and location of the trips was selected based on a detailed set of force and surface pressure measurements involving 20, 24, and 36 grit trips placed at multiple chordwise locations. All trips were able to eliminate the leading edge separation bubble related to the relatively low freestream Reynolds number. The pressure distributions were not otherwise notably changed, and the trips only modestly increased drag. In addition, lift slightly decreased and the lift versus angle of attack curve was linearized as opposed to its slope gradually decreasing. These trends followed the work of Mueller and Batill [33], which was not an important factor for these experiments. Moreover, the model was attached to a boundary layer fence, which was offset from the floor of the tunnel to inhibit interaction with its boundary layer.

The model was equipped with twelve finite span synthetic jet actuators mounted just upstream of the control surface hinge-line, labeled sequentially from the tip to the root of the model. Each jet had a rectangular orifice with a $1 \times 19.1$ mm cross-section and was driven by a piezoelectric disk that was sealed to a cavity. Furthermore, the jets were aligned such that their initial trajectory was $20^\circ$ from the model centerline plane, and the projection of their trajectory onto the model centerline plane was perpendicular to the hinge-line (i.e., offset by $34.5^\circ$ with respect to the freestream). The actuators were spaced as closely together in the spanwise direction as possible, which for the present experiments was an average of 41.8 mm (52% of the mean control surface chord) with every jet active. When every other jet was activated, the average spacing was 84.2 mm or 105% of the mean control surface chord. Note that the jets were arranged in groups of three, and the spacing between jets in different groups was slightly larger than those in the same group. The grouping was based on size limitations of the parts that could be manufactured with the stereolithography three-dimensional (3D) printer, which was selected to have a relatively high resolution while also limiting the number of modules that formed the wind tunnel model. Moreover, in the streamwise direction, the centers of each orifice were 7.7 mm upstream of the control surface hinge-line (9.6% of the mean control surface chord).

The synthetic jets were calibrated in quiescent conditions with a single hot-wire placed in the center of the orifice in the jet's spanwise direction. In the jet's streamwise direction, the hot-wire location was translated to the point where the peak velocities during the blowing and suction cycles were equal. The ratio of the peaks was measured, and a ratio of less than or equal to 1.03 was deemed acceptable. This location was observed to approximately be at the exit of the orifice.

The synthetic jets' average orifice velocity is given in Eq. (1), where $u_j(t)$ is the phase-averaged jet velocity and $T$ is the period of oscillation. The jets' strength was quantified using the area-based momentum coefficient and the blowing ratio, given in Eqs. (2) and (3), respectively. The former parameter relates the jets' momentum to the freestream momentum, where $A_j$ is the cross-sectional area of the jets' orifices and $n$ is the number of active jets. The latter equation is the ratio of the average jet velocity and the freestream velocity. In addition, $F^+$ is used as the jets' dimensionless frequency $f$ and is given in Eq. (4). Here, the jets' frequency was held constant at $f = 1600$ Hz for the present experiments, which corresponded to $F^+ = 21.7$. Note that this frequency is an order of magnitude larger than any of the dominant frequencies in the flow (e.g., the characteristic frequency, which was roughly 250 Hz based on the time of flight over the control surface):

$$U_j = \frac{1}{T}\int_0^{T/2} u_j(t)dt, \tag{1}$$

$$C_\mu = \frac{nU_j{}^2A_j}{1/2U_\infty{}^2S}, \tag{2}$$

$$C_b = \frac{U_j}{U_\infty}, \tag{3}$$

$$F^+ = \frac{f\bar{c}}{U_\infty}. \tag{4}$$

The main measurement technique used in the present experiments was stereoscopic particle image velocimetry (SPIV). SPIV was conducted using a New Wave Solo double-pulsed 120 mJ Nd:YAG laser and two LaVision Imager Intense thermoelectrically cooled, 12-bit CCD cameras with a resolution of $1376 \times 1040$ pixels and $532 \pm 10$ nm band pass filters. There were two main sets of experiments. The first, which will be referred to as the zoomed-out experiments, focused on the control surface and had a measurement domain that encompassed a spanwise region corresponding to the trajectory of approximately two to three synthetic jets. These experiments were conducted during multiple wind tunnel entries at two spanwise locations, centered around jets 5 and 9. The position of the measurement domains is shown in Fig. 1.

The cameras were equipped with lenses that had fixed focal lengths of 60 mm and were oriented such that there was roughly a 45° angle between them. They were placed on an optical table upstream of the model at an angle in which the surface near the hinge-line blocked the strongest intensity laser reflections from the surface. Care was taken such that the strength of the reflection line visible to the cameras was minimized, but not so much that data were lost near the surface. In this way, the strength of the laser could be turned up, the intensity of the particles increased, and the quality of the data enhanced. Moreover, Scheimpflug adaptors were installed between the cameras and lenses to correct for image distortion associated with the camera angles (Prasad [34]).

The laser was mounted on an optical table next to the tunnel, and the sheet penetrated through the sidewall. The sheet was created with a $-20$ mm cylindrical lens and was defocused slightly, such that the width at its waist was roughly 2 mm. The motivation behind this was to adequately capture the out-of-plane velocity component. Therefore, the time between laser pulses $\Delta t$ was limited by the thickness of the laser sheet, and, in the present experiments, $\Delta t$ was 30 $\mu$s.

The cameras and laser lens were mounted to different three-axis Velmex Bi-Slide traversing systems with a repeatability of $\pm 4$ $\mu$m, which allowed for measurements to be acquired at multiple locations. Also, water-based smoke particles $O(1$ $\mu$m) were generated using a theatrical fog machine placed near the tunnel's inlet and was used to seed the flow.

Data were acquired in planes parallel to the control surface hinge-line and normal to it near its mid-chord. Planes were taken in 2 mm increments from 2 mm downstream of the hinge-line to the trailing edge of the control surface, which was 86 mm and 66 mm downstream of the hinge-line for the inboard and outboard locations, respectively. Due to the unusual orientation in which measurements were obtained, data will be discussed using two sets of axes: the wind tunnel and the hinge-line axes (the global and local coordinate systems, respectively). The wind tunnel axes were composed of streamwise $x$, wall-normal $y$, and spanwise $z$ directions, whereas the hinge-line coordinates were in directions perpendicular to the hinge-line $x_{hl}$, parallel to the hinge-line $z_{hl}$, and their normal $y_{hl}$. All distances were nondimensionalized based on the synthetic jet orifice width of $w = 1$ mm, and the origin was the orifice center of jet 5 and jet 9 in the respective regions. Also, based on the orientation of these planes, the hinge-line was 11 mm downstream of the jets' orifices (e.g., the plane of data farthest upstream was acquired at $x_{hl}/w = 13$). Outboard, in the $z_{hl}$ direction, each plane encompassed a region approximately 36 mm inboard and 126 mm outboard from the projection of the center of jet 5's orifice. Similarly, the inboard planes surrounded a region that was 27 mm inboard and 108 mm outboard of jet 9.

Data were acquired with no jets active (baseline), a single jet active, every other jet active, and all jets active. Moreover, time-averaged and phase-averaged measurements were taken over 500 image pairs, where the phase-averaged cases were taken at two phase angles with respect to the synthetic jet's sinusoidal input voltage, $\varphi = 120^\circ$ and $240^\circ$. A phase of $0^\circ$ corresponded to the zero crossing with a positive slope.

The other set of SPIV experiments, the zoomed-in cases, were focused in the vicinity of a single synthetic jet, where the higher spatial resolution allowed for the flow physics to be analyzed in greater detail. For these cases, the model was mounted on the side wall of the tunnel to facilitate an easier setup (typically wind tunnel models were assembled to the tunnel floor). The cameras were mounted on the optical table, and the laser was below the tunnel. The angle between the cameras was about $30^\circ$, the camera lenses had fixed focal lens of 200 mm, and $\Delta t$ was 5 $\mu$s.

The planes were centered around jet 5 and angled perpendicular to the leading edge. The measurement domain was from approximately 10 mm upstream to 30 mm downstream of the jet's orifice (in the $x_{le}$ direction). Since a smaller region needed to be illuminated relative to the zoomed-out tests, the laser light sheet was focused to a width of about 1 mm with a $-50$ mm cylindrical lens, which spread the sheet more gradually (relative to a $-20$ mm lens). The cameras and laser were traversed parallel to the hinge-line, and planes were acquired in 1 mm increments from 12 mm inboard of the orifice's center to 28 mm outboard. In addition, time-averaged and phase-averaged data were taken over 500 image-pairs. Phase-averaged measurements were acquired starting at a $0^\circ$ phase angle and in $60^\circ$ increments.

The velocity field was computed from the cross-correlation of successive image pairs with a 75% overlap between interrogation domains. A larger overlap was used, relative to a 50% overlap, to increase the spatial resolution. Images were processed with two initial correlation passes of $64 \times 64$ and two final passes of $32 \times 32$ pixels using the most accurate methods available in the DaVis 8.1 software. A Matlab program was used to compute the average velocity field ($U$, $V$, $W$) for each plane from the instantaneous velocity fields and assemble all the planes into a flow volume. Vorticity fields

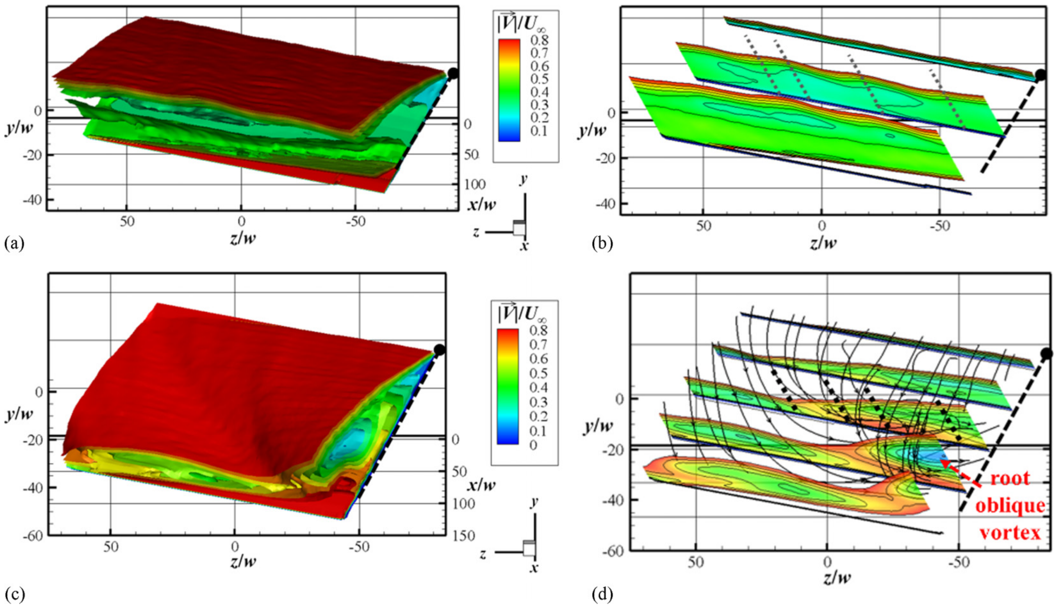


FIG. 2. Baseline flow field at the (a), (b) outboard, and (c), (d) inboard zoomed-out regions. (a), (c) Isosurfaces of normalized total velocity, and normalized total velocity contours at (b) $x_{hl}/w = 13$, 44, and 75 for the outboard location and (d) $x_{hl}/w = 17$, 37, 57, 77, and 97 for the inboard location. 3D streamlines are superimposed in panel (d).

were also computed with the software. The error in pixel displacement was estimated to be roughly 0.2 pixels. The error associated with the freestream velocity was estimated to be $\pm 1.43$ m/s and $\pm 0.77$ m/s for the zoomed-in and zoomed-out cases, respectively.

## III. RESULTS

As discussed above, SPIV data were acquired in regions surrounding the trajectories of jets 5 and 9, which will be referred to as the outboard and inboard regions, respectively. These locations were selected because the severity of separation in the baseline flow field was considerably different, as will be shown later. Section III A discusses the baseline flow field, where Secs. III B and III C discuss the interaction of a single synthetic jet and an array of jets, respectively, with the crossflow at both spanwise locations.

### A. Baseline flow fields: Inboard and outboard regions—Zoomed-out

The baseline flow field over the control surface is initially discussed. Figures 2(a) and 2(b) show data collected at the outboard location and Figs. 2(c) and 2(d) present the results at the inboard region. Isosurfaces of normalized total velocity, $|\vec{V}|\ /U_\infty$, are presented in Figs. 2(a) and 2(c), and multiple planes of normalized total velocity contours, superimposed with 3D streamlines, are shown in Figs. 2(b) and 2(d) at both locations. The figures are oriented such that the model is being viewed from a downstream location. Therefore, the freestream is primarily coming out of the page, the outboard side of the model (negative $z$ direction) is on the right, and the inboard side is on the left. The dashed black line represents the control surface, and the black dot is its hinge-line, and the dotted lines are the spanwise locations where velocity profiles were extracted, as will be shown later.

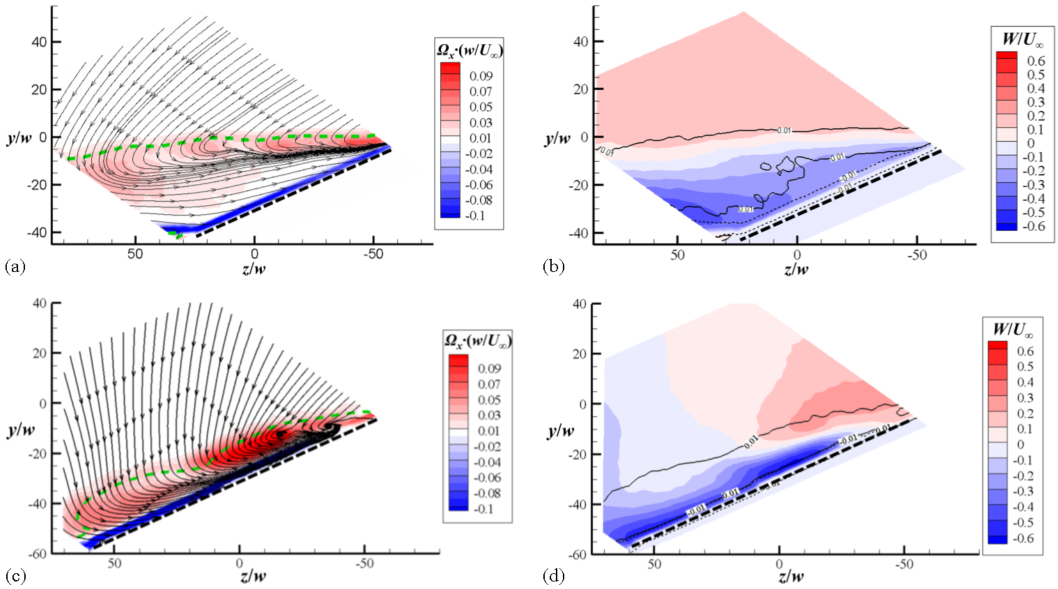

FIG. 3. Baseline flow field presented in planes perpendicular to the streamwise direction at $x/w = 56$ for the (a), (b) outboard and (c), (d) inboard zoomed-out regions. (a), (c) Color contours of normalized streamwise vorticity superimposed with in-plane streamlines (the green dash line corresponds to $|\vec{V}|/U_\infty = 0.7$); (b), (d) color contours of normalized spanwise velocity superimposed with line contours of normalized streamwise vorticity.

In the outboard region, the isosurfaces lift off of the surface with downstream distance, suggesting that the flow has separated. Velocity profiles (which will be shown later) confirm that the flow has actually separated. In addition, the separation is fairly uniform in the $z_{\rm hl}$ direction, suggesting that at this measurement domain the flow is not severely affected by the model's 3D end effects (e.g., the tip vortex and the horseshoe vortex). Last, low spanwise undulations can be seen in the isosurfaces due to the presence of the synthetic jet orifices (even though they were not actuated). Experiments, not presented here for brevity, with orifices that were taped closed show a negligible change in the side force relative to orifices that were open and inactive.

Data acquired in the inboard region also show that the isosurfaces pull off of the surface, indicative of flow separation. Again, it will be demonstrated that the flow is separated using velocity profiles later in the paper. Other than this though, the baseline flow field at this region is much different than in the outboard region of the control surface. For one, the wall-normal distance of the isosurfaces from the surface varies fairly significantly along the span, where the separation is more severe in the outboard direction. In general though, separation is less severe in the inboard region compared to the outboard region. This was also observed in the surface pressure and tuft flow visualizations from our previous experiments (Rathay *et al.* [35]) as well as in other work (Greenblatt and Washburn [24]). Moreover, the 3D streamlines exhibit a vortex near the outboard edge of the measurement domain, which is a root oblique vortex, as was discussed in detail in Jansen *et al.* [32].

To gain additional insight into the details of the baseline flow field, data at a spanwise plane (i.e., perpendicular to the streamwise direction) of $x/w = 56$, are shown in the outboard [Figs. 3(a) and 3(b)] and inboard [Figs. 3(c) and 3(d)] regions. In Figs. 3(a) and 3(c), the color contours represent normalized streamwise vorticity, $\Omega_x \cdot w/U_\infty$, superimposed with in-plane streamlines and a green contour line corresponding to $|\vec{V}|\ /U_\infty = 0.7$. Figures 3(b) and 3(d) present the normalized spanwise velocity, $W/U_\infty$, superimposed with lines of normalized streamwise vorticity. Note that the dashed black line represents the surface, which cuts through the plane at an irregular angle. This angle is an artifact of the control surface hinge-line and streamwise direction not being perpendicular to one another. Consequently, the distance from the hinge-line to the plane varies in the spanwise direction.

The vorticity field at the outboard region [Fig. 3(a)] exhibits a region of positive (counterclockwise) vorticity that is associated with the separated shear layer. Within the separated region, the streamlines also clearly illustrate the spanwise crossflow that is oriented toward the tip of the model. Figure 3(b) shows that the spanwise velocity is quite large; at this particular plane it is a maximum of 44% of the freestream. Inboard, the results are different, as expect. At all spanwise locations, the total velocity contour line is closer to the surface [Fig. 3(c)] than it is in the outboard measurement domain. In addition, there is a recess in the line; this feature divides regions of mild and more severe flow separation inboard and outboard, respectively. As mentioned earlier, the stronger separation in the outboard side of the inboard region corresponds to a vortex, which is visible in the streamlines. However, this structure is angled toward the tip (relative to the $x$ direction) and appears smaller at this orientation that it actually is. The recirculating region is associated with a large concentration of positive $\Omega_x$, much stronger than corresponding $\Omega_x$ in the outboard measurement domain. Moreover, the negative spanwise velocity contours [Fig. 3(d)] are more concentrated near the surface at the inboard location, and their magnitude is also larger (a maximum of 63% of the freestream at this plane), which is related to the root oblique vortex [32]. As was shown by Jansen *et al.* [32], this vortex is created and rotated in the counterclockwise direction (in the given frame of reference), because of the differences in separation severity and the spanwise crossflow. Likewise, it is presumably important that the spanwise crossflow is negative near the surface (oriented outboard) and become increasing positive with distance from the surface in this region. This vortex augments the negative spanwise velocity near the surface further. Note that the tendency for this spiral vortex to form at different angles of attack, sweep angles, leading edge radius, and Reynolds numbers was explored extensively by Poll [36].

Next, the normalized turbulent kinetic energy ($\mathrm{TKE}/U_\infty^2$) of the baseline flow field was calculated for the flow volume and in $z_{\mathrm{hl}}$-$y_{\mathrm{hl}}$ planes that are presented in Figs. 4(a) and 4(c), and Figs. 4(b) and 4(d), respectively. Figures 4(a) and 4(b), and Figs. 4(c) and 4(d) correspond to the outer and inner regions, respectively. In the outer region, there is a concentration of TKE associated with the separated shear layer, with a relatively uniform magnitude of TKE. In the inboard region [Figs. 4(c) and 4(d)] the TKE increases in the outboard direction. This corresponds to the increase in severity of the flow separation in this region.

In summary, the flow field that the jets will interact with is significantly different at the respective locations. In the outboard region, separation is more severe and spanwise uniform, whereas inboard, the flow separation is weaker, but its severity varies along the span. As will be shown below, these differences greatly affect the jets' interaction with the flow over the control surface.

### B. Time-averaged flow fields: A single jet actuated

#### *1. Inboard and outboard regions—Zoomed-out*

The interaction of a single synthetic jet with the separated flow is first studied before the more complex cases involving arrays of jets are analyzed. This is initially discussed using the zoomed-out data. Then, the flow physics is studied with data acquired closer to jet 5's orifice. Figure 5 shows time-averaged normalized total velocity collected in the outboard and inboard regions with just jets 5 or 9 were activated with $C_b = 0.85$ ($C_\mu = 0.021\%$), respectively. The effect of a single jet in the outboard measurement domain is clearly visible in the isosurfaces and planes of total velocity [Figs. 5(a) and 5(b), respectively]. Downstream of the jet orifice (marked by the black line), separation is reduced, as indicated by a recess in the isosurfaces. Additionally, separation is reduced over the control surface outboard of the orifice, but there does not appear to be a beneficial effect inboard of the jet. In fact, there is actually a small velocity deficit around $z/w = 16$ (i.e., the jet adversely affects the flow here).

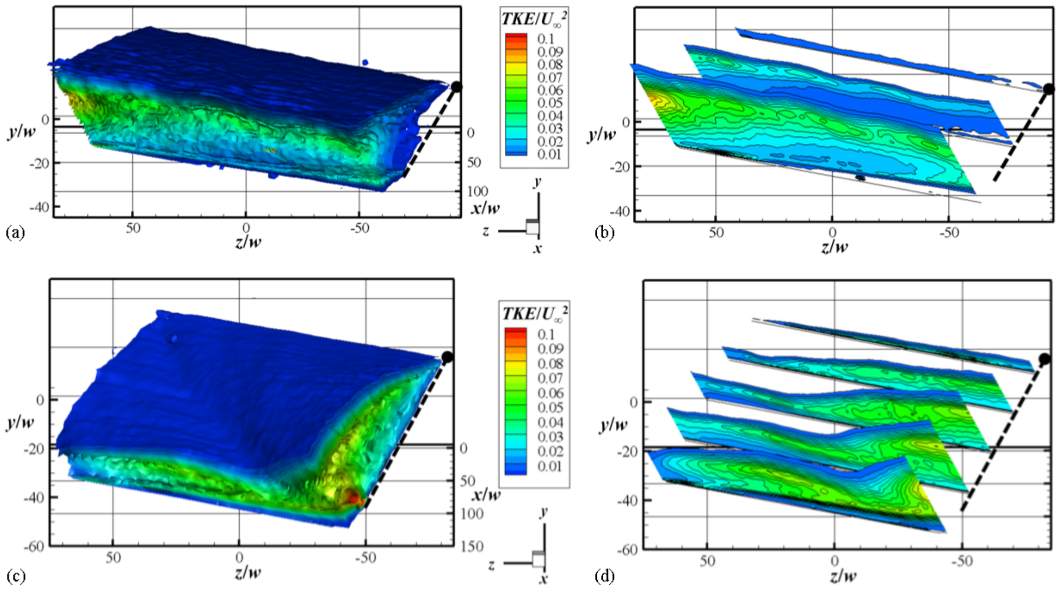

FIG. 4. (a), (c) Isosurfaces of $\mathrm{TKE}/U_\infty^2$, and (b), (d) $\mathrm{TKE}/U_\infty^2$ contours for the outboard and inboard regions, respectively. (b) Planes at $x_{\mathrm{hl}}/w = 13$, 44, 75, and (d) at $x_{\mathrm{hl}}/w = 17$, 37, 57, 77, 97. Zoomed-out set of experiments.

The most notable flow feature at the inboard location is a large ridge downstream of the orifice, which bends toward the streamwise direction [Figs. 5(c) and 5(d)]. This ridge also represents a velocity deficit, and outboard of the ridge separation is reduced. This is analogous to the results obtained at the outboard measurement domain; inboard the flow is closer to being attached though. Downstream of the orifice and in the vicinity of its trajectory the streamlines are turned in the freestream direction. Inboard of the jet, at $z/w > 40$, the streamlines are very similar to the baseline. Furthermore, outboard, the vortex visible in the baseline flow field is not clearly distinguishable in the measurement domain. Presumably, this region is pushed farther outboard when a single jet is activated.

The interaction domain between the synthetic jet and the flow over the control surface can also be explored by visualizing the trajectory of the jet using the time-averaged streamwise vorticity field as presented in Fig. 6. First, the effect of the synthetic jet at the outboard location is discussed. When jet 5 is active [Fig. 6(a)] the vorticity field is primarily composed of positive (counterclockwise) vorticity, which was observed in the baseline. Downstream of the jet orifice, however, there is a concentration of negative vorticity related to the synthetic jet that is visible until the trailing edge of the control surface. The $y$ and $z$ components of vorticity associated with the jet, not shown for brevity, dissipate more quickly and are not visible by the trailing edge.

The interaction of a single synthetic jet (jet 9) with flow over the control surface in the inboard region is discussed next and is shown in Fig. 6(b). Comparing to the interaction of the synthetic jet (jet 5) at the outboard region [Fig. 6(a)], the vorticity concentration associated with the synthetic jet diminishes (at these levels of $\Omega_x$) before the trailing edge of the control surface, which is a noteworthy difference with respect to the outboard measurement domain. It should be noted that the chord at the inboard region is larger, where the trailing edge is roughly $x_{\mathrm{hl}}/w = 86$ and 66 downstream of jets 9 and 5, respectively. However, this is not the sole reason for these differences, which is discussed in more detail below.

To further explore the streamwise vorticity created by a single synthetic jet, it is presented in Fig. 7 in planes similar to those from Fig. 3. At the outboard location [Fig. 7(a)], the negative

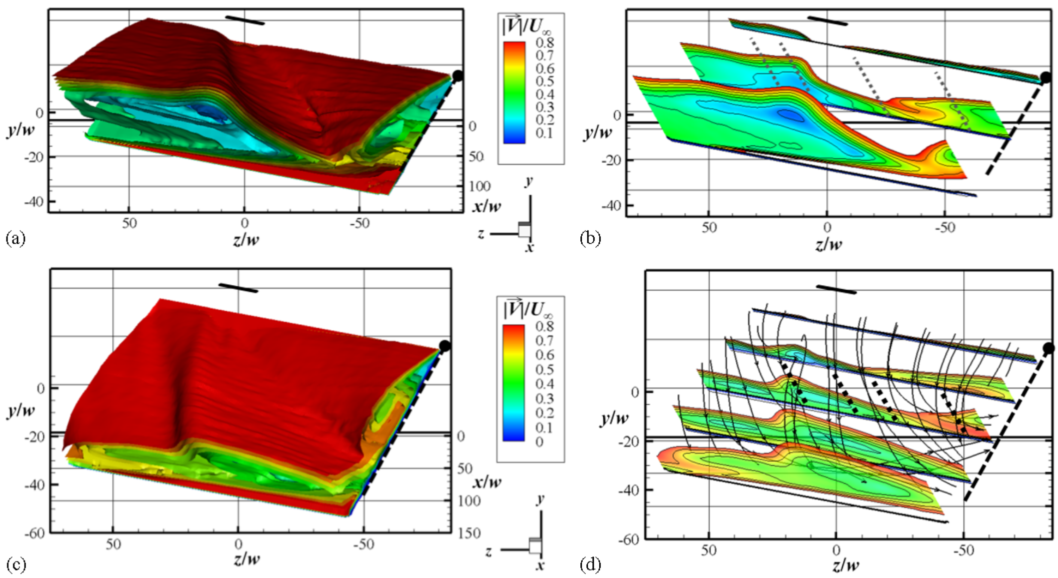


FIG. 5. Time-averaged flow field with a single jet active at the (a), (b) outboard and (c), (d) inboard zoomed-out regions. (a), (c) Isosurfaces of normalized total velocity, and normalized total velocity contours superimposed with 3D streamlines at (b) $x_{\mathrm{hl}}/w = 13$, 44, and 75 for the outboard location and (d) $x_{\mathrm{hl}}/w = 17$, 37, 57, 77, and 97 for the inboard location.

vorticity concentration related to the jet is visible around $z/w = 7$ and $y/w = -2$. The streamlines are directed toward the surface outboard of the concentration, and inboard the jet appears to create a virtual barrier, which inhibits some of the spanwise crossflow within the separated region and near the shear layer. The interaction of the barrier with the spanwise crossflow results in a recirculation region in some of the planes upstream of $x/w = 56$ (not presented for brevity) and is related to the velocity deficit observed in the isosurfaces of total velocity (Fig. 5). Beneath the negative concentration, many of the streamlines within the separated region converge. Moreover, there is a large concentration of positive vorticity located just outboard of the recess ($z/w > 20$) where the proximity of the total velocity contour line from the wall is increasing (i.e., separation is becoming more significant). This appears to resemble the flow field associated with the vortex observed in the inboard region of the baseline case, where separation severity is greatly increasing. Indeed, there is a vortex in the outboard region when a single jet is active that rotates in the counterclockwise

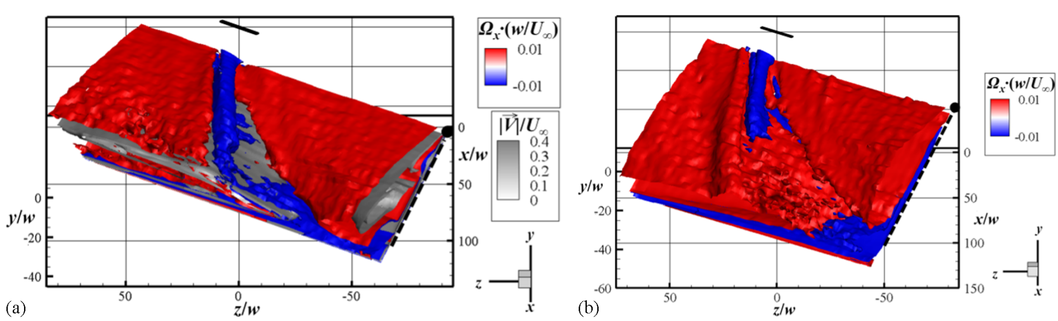


FIG. 6. Isosurfaces of time-averaged normalized streamwise vorticity with (a) a single jet (jet 5) active at the outboard location and (b) jet 9 active at the inboard location.

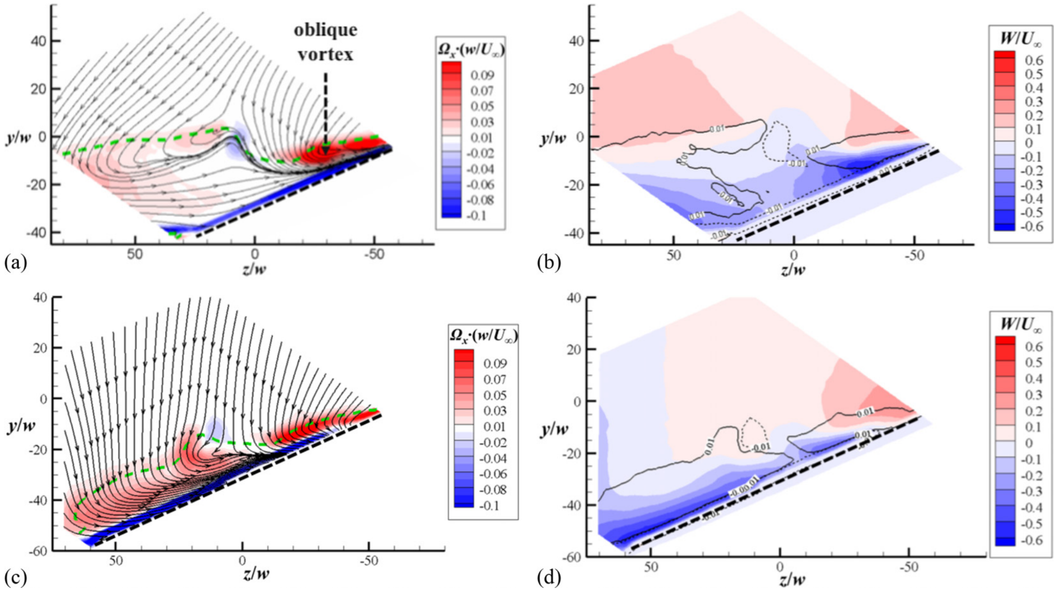


FIG. 7. Time-averaged flow field with a single jet active presented in planes perpendicular to the streamwise direction at $x/w = 56$ for the (a), (b) outboard and (c), (d) inboard zoomed-out regions. (a), (c) Color contours of normalized streamwise vorticity superimposed with in-plane streamlines and a green contour line corresponding to $|\vec{V}|/U_\infty = 0.7$, and (b), (d) color contours of normalized spanwise velocity superimposed with line contours of normalized streamwise vorticity.

direction and travels along an oblique line with respect to the freestream. The importance of this vortex and how it is formed is discussed in more detail in our previous work (Jansen *et al.* [32].), and based on its trajectory, is referred to as the oblique vortex.

This vortex is believed to be primarily responsible for spanwise velocity being further increased near the surface and outboard of the jet structures [Fig. 7(b)]. The maximum spanwise velocity at this plane is approximately 50% of the freestream, which occurs at $z/w = -28$ and is a considerable increase relative to the baseline flow field. It was shown by Jansen *et al.* [32]. that the magnitude of the spanwise velocity $W$ reaches a maximum directly below the oblique vortex. Furthermore, inboard of the single jet, the spanwise velocity is lower than in the baseline, which is believed to be associated with the virtual barrier in this region.

In the inboard region at $x/w = 56$, the negative vorticity related to jet 9 (when it is solely active) is visible at $z/w = 11$ [Fig. 7(c)]. However, it is weaker relative to the same feature in the outboard region [Fig. 7(a)], which might be related to the stronger spanwise crossflow in the baseline flow field (i.e., its interaction with the crossflow vortex). Inboard of the jet, there is a peak in positive $\Omega_x$ as well, which is just inboard of the negative jet concentration ($z/w = 11$, $y/w = -12$) and corresponds to the location of a peak in the total velocity contour line (i.e., where separation is more severe). Outboard and near jet 9, the flow is angled downward toward the surface. Also, in comparison to both the baseline flow field inboard of the jet and the actuated flow field in the outboard region, the positive streamwise vorticity at the outboard edge of the inboard measurement domain is not as strong. This is presumably because there does not appear to be a large vortex at the location where separation severity is increasing; likely since the baseline separation is milder inboard, and therefore the change in separation severity is much smaller than in the outboard measurement domain. Furthermore, the magnitude of the spanwise velocity component is reduced outboard of the jet's structures [Fig. 7(d)] in comparison to the baseline. These results are also different than those obtained at the outboard measurement location, where the magnitude

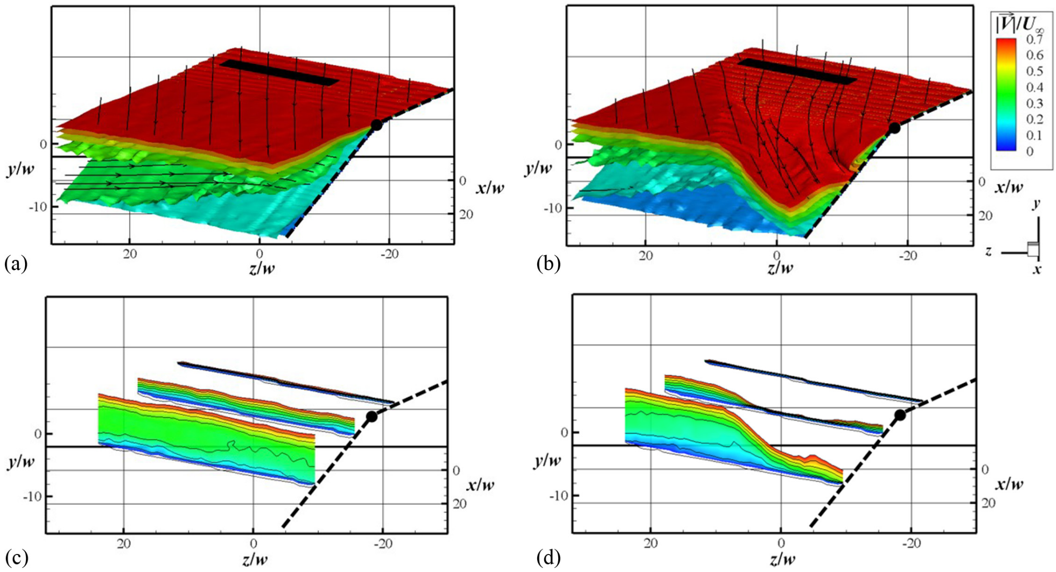


FIG. 8. Time-averaged flow field in the vicinity jet 5's orifice: (a), (c) baseline, and (b), (d) jet 5 is active. (a), (b) Isosurfaces of $|\vec{V}|/U_\infty$ superimposed with streamlines above the jet's orifice and near the control surface. (c), (d) Velocity contours of $|\vec{V}|/U_\infty$ in planes perpendicular to the hinge-line at $x_{\mathrm{hl}}/w = 2.4$, 11, and 19.6. Zoomed-in set of experiments.

of spanwise velocity increases outboard of the recess in total velocity, and also can be attributed to a crossflow vortex that is either nonexistent or indistinguishable in the data.

The effect of a single synthetic jet at the outboard and inboard regions can be summarized as follows. At the outboard location, jet 5 reduces the separation, but it is not capable of completely reattaching the severely separated flow. Additionally, outboard of the recess in total velocity, where separation is significantly varying and approaching the separation severity of the baseline case, the flow field is characterized by a large vortex that appears to further enhance the spanwise velocity. At the inboard location, jet 9 also reduces separation, more so than in the outboard region. There is no distinguishable crossflow vortex at this location though, and the spanwise velocity magnitude is reduced. At both locations, the jets are associated with negative (clockwise) concentrations of vorticity, which is slightly larger in the outboard region.

### *2. Single jet actuated: Outboard region—Zoomed-in*

To further explore the interaction of jet 5 with the flow over the control surface at the outboard location, data were collected at a smaller domain encompasses jet 5 (zoomed-in region, see Fig. 1). First, the mean flow fields with and without the activation of jet 5 is presented. Isosurfaces of the total velocity (normalized by $U_\infty$) superimposed with streamlines are shown in Fig. 8(a). Streamlines are given at two locations to demonstrate the direction of the flow over the jet orifice and the control surface. The thick, dashed lines represent the main element and control surface, which are separated by a black dot, symbolizing the hinge-line. The rectangular black box represents the jet orifice. This figure is presented in the wind tunnel global axes ($x$, $y$, $z$), and it is oriented such that the streamwise, $x$, direction is out of the page and the spanwise, $z$, direction is from right to left (right being outboard). The origin of this coordinate system is the center of jet 5's orifice. Figure 8(c) shows contours of $|\vec{V}|$ in planes perpendicular to the hinge-line at $x_{\mathrm{hl}}/w = 2.4$, 11, and 19.6. Note the origin of the coordinate system is the jet orifice's center as well.

The isosurfaces of $|\vec{V}|$ lift off of the control surface with downstream distance, indicating that the flow has separated, and as expected, separation commences at the control surface hinge-line. Furthermore, the streamlines, which originate on the main element, show that in the vicinity of the orifice the flow is angled slightly inboard and as it moves over the control surface it bends in the outboard direction. However, streamlines located in the separated region over the control surface have a significant spanwise component due to the sweep angle of the model; they are oriented roughly in the hinge-line direction.

The effect of activating a single jet (jet 5) at $C_\mu = 0.021\%$ ($C_b = 0.85$) on the time-averaged flow field is presented using isosurfaces of total velocity superimposed with streamlines [Fig. 8(b)] and in planes perpendicular to the hinge-line [Fig. 8(d)]. The jet pulls the flow closer to the surface (as can be seen by the recess in the isosurfaces) downstream and outboard of its orifice, signifying that separation is reduced at these locations. Also, within the recess in the isosurfaces, there are two smaller depressions. Furthermore, the streamlines that pass over the orifice turn inboard at first, in the direction of the initial jet trajectory and then turn into the streamwise direction. The streamlines in the separated region over the control surface, which were originally parallel to the hinge-line, appear to turn downstream in the recess. Inboard of this location, the jet does not appear to have a significant influence. Figure 8(d) also clearly demonstrates that separation is reduced downstream and outboard of the jet orifice.

The mechanism by which the activation of the synthetic jet reduces the separation downstream and outboard of its location was further explored using phase-locked data. As is well known, the synthetic jet is unsteady in nature; thus, in order to explore the interaction and evolution of the jet with the flow, one needs to examine the phase-averaged flow field so that the vortical structures issued from the synthetic jet can be better analyzed and understood. Therefore, phase-locked measurements were conducted and are primarily used to investigate the formation, advection, and interaction of jet 5 with the crossflow. These data were acquired at six different phases from $0^\circ$ to $300^\circ$ in $60^\circ$ increments. Note that the phase was measured with respect to the driving signal. Isosurfaces of total vorticity, $|\Omega|$, and total velocity, $|\vec{V}|/U_\infty$, are presented together in Fig. 9. The gray isosurface corresponds to $|\Omega| = 0.4$ and the other isosurfaces represent $|\vec{V}|/U_\infty$.

The ejection of the synthetic jet into the crossflow is first observed in $|\Omega|$ at $\phi = 180^\circ$ [Fig. 9(d)]. An elongated vortex ring is formed at the orifice where the vorticity is generated at the long sides and at the edges of the orifice. During the beginning of the cycle of the synthetic jet, the vortex ring advects downstream, stays close to the wall, and appears to maintain its original trajectory and orientation [Figs. 9(e) and 9(f)]. Initially, on the airfoil surface, the portion of the ring formed at the long, upstream orifice edge (upstream leg) is the strongest (not shown here for brevity but was determined from quantitative evaluation of $|\Omega|$). At $\phi = 0^\circ$ [Fig. 9(a)], the vortex ring is close to the hinge-line and resembles a well-defined elliptical vortex ring. The legs of the ring formed at the edges are farther downstream, which resembles axis switching in rectangular jets in quiescent conditions (Grinstein [37] and Van Buren *et al.* [11]. Moreover, the shallow pitch angle of the jet is also apparent here, based on the location of the spanwise portions of the ring with respect to one another (i.e., the upstream leg is farther away from the wall compared to the downstream leg). As the ring advects over the hinge-line and is subjected to the strong spanwise crossflow over the control surface [as was discussed in Fig. 7(b)] the vortex ring quickly deforms. The downstream advection of the inboard edge of the vortex ring is slower in comparison to its outboard edge. In addition, the inboard portion of the ring quickly diminishes in strength, whereas the outboard side is more resilient to the crossflow. This is apparent in Figs. 9(c) and 9(d) and is partially because the crossflow interacts more with the inboard portion of the ring. Also, the outboard portion of the vortex ring is initially stronger, because of the skew angle. At $\phi = 240^\circ$ [Fig. 9(e)] the inboard portion of the ring has dissipated to the point that it appears disconnected at this end. Then, at $\phi = 0^\circ$ [Fig. 9(a)], approximately $540^\circ$ since the jet was observed exiting the orifice, the spanwise legs (which were the strongest at first) have disappeared, and the only visible vorticity concentration is that associated with the outboard edge. This concentration now resembles a sideways horseshoe vortex that advects downstream until it leaves the measurement

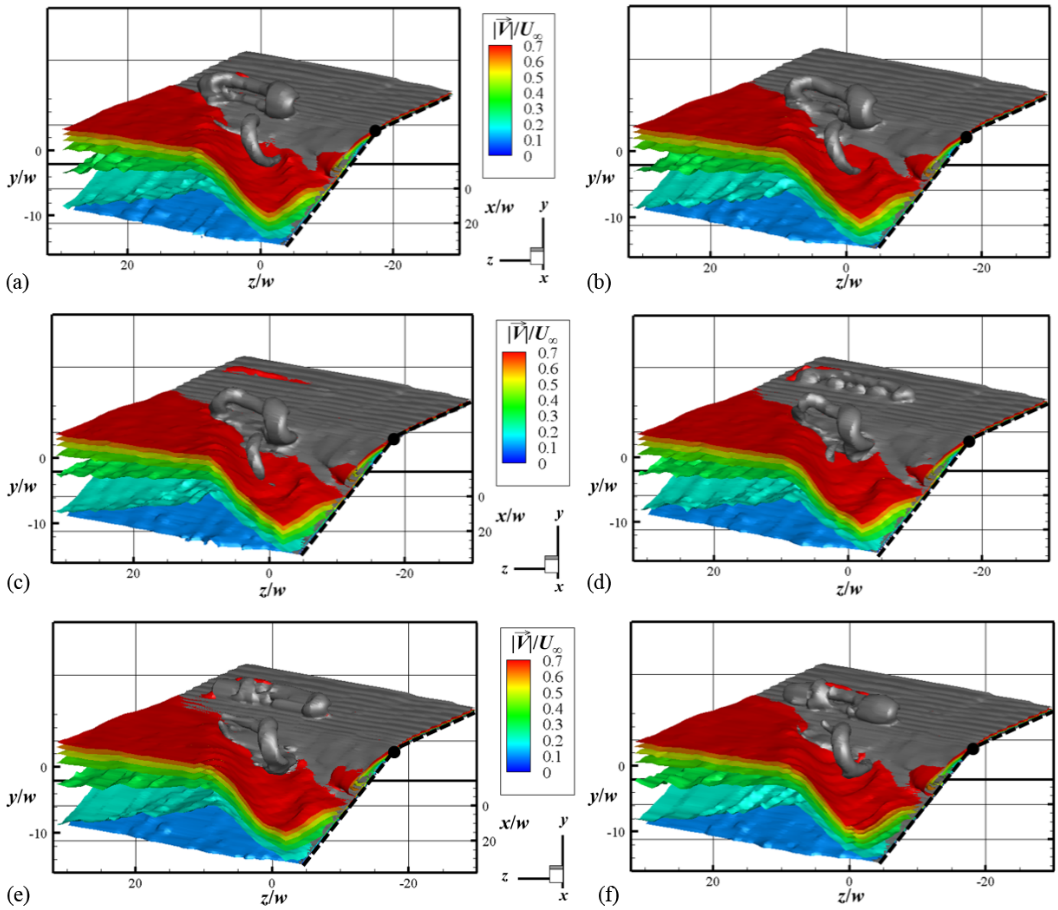

FIG. 9. Phase-averaged flow field in the vicinity Jet 5's orifice with it active. The gray isosurfaces correspond to $|\Omega| = 0.4$ and the other isosurfaces represent $|\vec{V}|/U_\infty$. The data are shown at multiple phases of the synthetic jet cycle: (a) 0°, (b) 60°, (c) 120°, (d) 180°, (e) 240°, and (f) 300°.

domain. Note also that the disappearance of the isosurface of total vorticity does not necessary mean that the vortex ring has been entirely annihilated. If the value of the $|\Omega|$ isosurface was decreased, part of the ring that seems to have vanished would be visible, but concurrently it would be more difficult to distinguish from the crossflow (hence why this value was chosen). These data, instead, demonstrate that on the control surface the outboard portion of the vortex ring has the largest vorticity concentration, which is believed to be important in reducing separation in this flow field.

Another way to present the phase-locked data is at different 2D planes. Figure 10 presents $x$-$y$ planes of superimposed phase-locked total velocity contours, $|\vec{V}|\ /U_\infty$, with isosurfaces corresponding to $|\Omega| = 0.4$ at four $z$ locations. Note that only $\phi = 240°$ is presented for brevity, but the flow features are similar at the other phases. At $z/w = 10$ [slightly inboard of the vortical structures issued from the jet, Fig. 10(a)], the vortical structures are behind the plane at this viewing angle. There are a couple of bumps in the contours at roughly $x/w = -2$ and 14, which are just inboard of the vortex rings. Hence, their interaction with the spanwise crossflow creates a velocity deficit. Farther outboard, at $z/w = 6$ [Fig. 10(b)], the plane is through two vortex rings; the inboard side of the upstream ring and the center of the downstream vortical structure. Note that at this location, the plane mainly intersects with the spanwise legs of the rings. Upstream (at $x/w = -2$), the jet enhances the velocity near the wall and creates a deficit above it. The deficit is a result

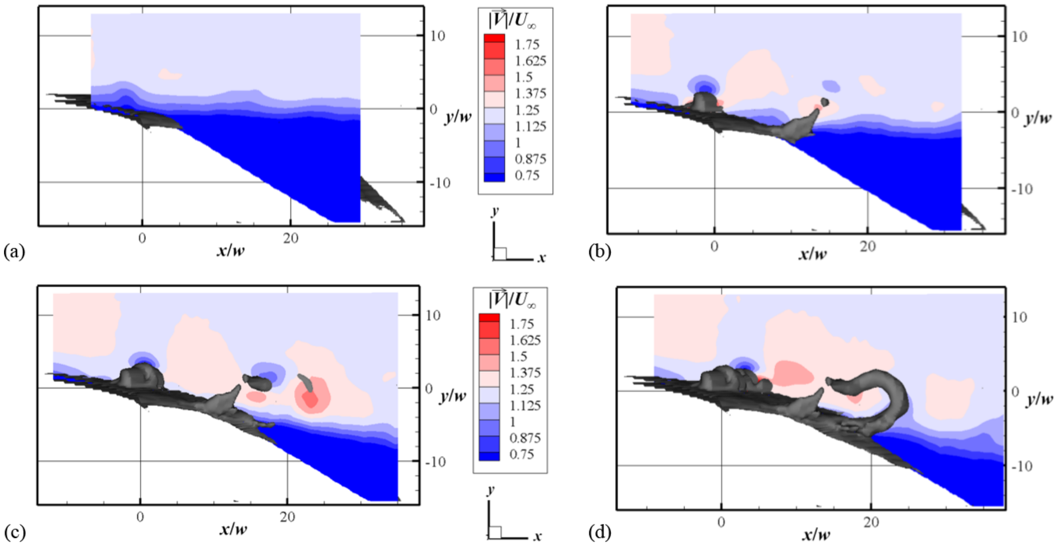


FIG. 10. Phase-averaged measurements in *x*-*y* planes at $\phi = 240^\circ$ in the vicinity of the orifice of jet 5. The gray isosurfaces correspond to $|\Omega| = 0.4$ and the colored contours represent $|\vec{V}|/U_\infty$. $z/w =$ (a) 10, (b) 6, (c) 2, and (d) $-2$. Zoomed-in set of experiments.

of the counterclockwise spanwise vortex motion interacting with the crossflow moving from left to right (from this viewing angle). Furthermore, at the location of the downstream vortex ring, there are similar, but weaker effects on $|\vec{V}|$. At $x/w = 13$ and $y/w = 1$, which is the middle of the counter-rotating spanwise legs, the velocity is higher than the baseline value, and it is lower above the upper leg (in *y*). At $z/w = 2$ [Fig. 10(c)], the plane intersects the center of the upstream ring and is inboard of the outboard side of the downstream ring, the latter of which significantly enhances the velocity in its vicinity (at this spanwise location). Moreover, the total velocity also increases between the two vortex rings. Finally, $z/w = -2$ is shown in Fig. 10(d), which is on the outboard side of the upstream ring and just outboard of the downstream ring. The downstream ring, which resembles a horseshoe, primarily rotates in the *x* direction. Near the surface at this location, the rotation lifts the flow up and creates a reduction in $|\vec{V}|$. However, between and above the outboard edge of the vortex ring there is still an increase in the velocity.

Another parameter that can aid to further explore the evolution and advection of the vortical structures is the phase-averaged spanwise vorticity, which is plotted in *x*-*y* planes and presented in Fig. 11. These data are given at two phases of the synthetic jet cycle ($\phi = 120^\circ$ and $240^\circ$), and at two planes ($z = 0$ and 4). The outboard plane ($z = 0$) is in the center of the jet orifice, and therefore, near the orifice it is roughly in the middle of the spanwise-oriented sides of the vortex ring. Additionally, on the control surface, the plane is approximately in the middle of the horseshoe shaped, outboard edge of the vortex ring. At this location and for $\phi = 120^\circ$ [Fig. 11(a)], vorticity associated with the outboard portion of the ring is present around $x/w \approx 12$. There are two distinct concentrations of positive vorticity, which are from a single vortex ring that is warped. At the second phase [$\phi = 240^\circ$, Fig. 11(b)], the positive concentrations have spread, because the ring has warped more. There is a concentration of negative $\Omega_z$ above the positive concentrations that is also associated with the ring warping and the separated shear layer. Furthermore, upstream, the spanwise sides of the ring are visible and appear to be within the boundary layer. The upstream side is also much stronger than the downstream one.

The inboard plane ($z/w = 4$) intersects the vortex rings on the control surface across their long side, and the vorticity field resembles that of a typical 2D synthetic jet. At $\phi = 120^\circ$ [Fig. 11(c)], there is a strong concentration of positive $\Omega_z$ around $x/w = 10$ with weaker, negative $\Omega_z$

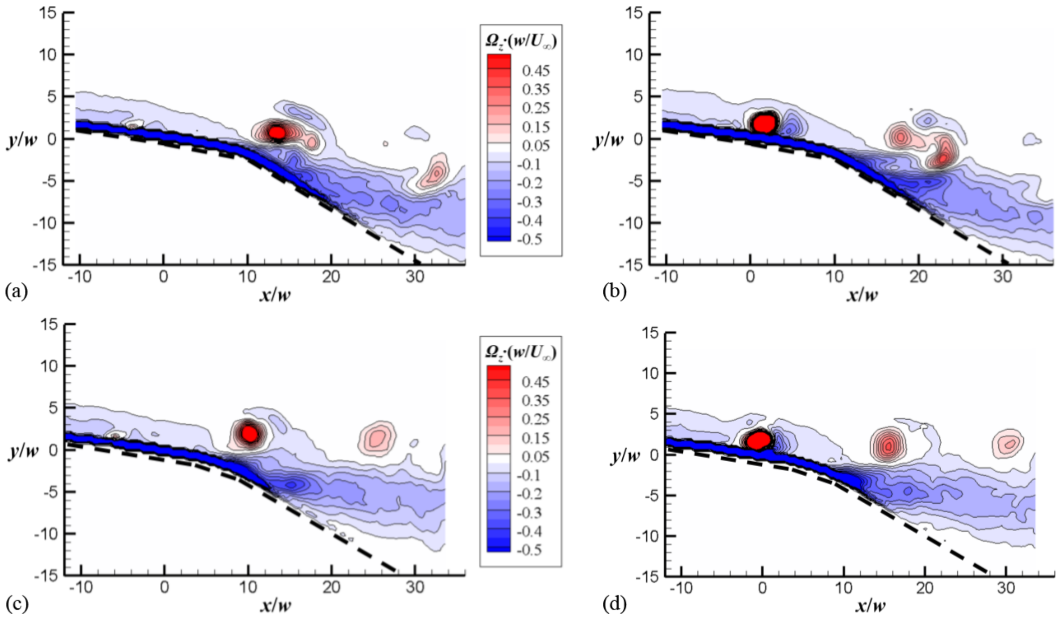


FIG. 11. Contours of phase-averaged $\Omega_z\, w/U_\infty$ in $x$-$y$ planes at $\phi =$ (a), (c) 120° and (b), (d) 240°. The data are shown at $z/w =$ (a), (b) 0 and (c), (d) 4. Zoomed-in set of experiments.

downstream of it. The positive concentration is fairly circular (much different than what was observed outboard), and it significantly decreases in strength when it reaches $x/w = 26$ after one cycle, which is because it is opposing the freestream direction and crossflow vorticity. Moreover, similar circular positive concentrations are distinguishable at $\phi = 240°$ [Fig. 11(d)].

### C. Time-averaged flow fields: An array of jets actuated

This section primarily focuses on two jet configurations: (1) every other jet active and (2) all jets active. These configurations were compared to each other at both spanwise measurement domains, as well as to the baseline and when only a single jet was active. The lift coefficient for these conditions is given in Table I. Lift augmentation increases with the number of active jets. However, there is not a large difference in the lift coefficient for cases where every other jet and all jets are active even though the momentum coefficient differs by a factor of two. The flow physics associated with these global measurements is discussed below; the interaction of multiple arrays of synthetic jet actuators with a severely separated crossflow and with each other in a highly 3D flow field is explored.

First, the effect of every other jet (odd numbered jets) actuated at $C_b = 0.85$, which corresponds to $C_\mu = 0.124\%$, is investigated and is presented in Fig. 12, which shows isosurfaces of $|\vec{V}|\ /U_\infty$ [Figs. 12(a) and 12(c)], and contours of $|\vec{V}|\ /U_\infty$ in multiple planes parallel to the hinge-line and

TABLE I. Lift coefficient for different synthetic jet operating conditions.

| Condition | $C_L$ |
|---|---|
| Baseline | 0.73 |
| Only jet 5 is on | 0.76 |
| Every other jet is on | 0.84 |
| All jets are on | 0.87 |

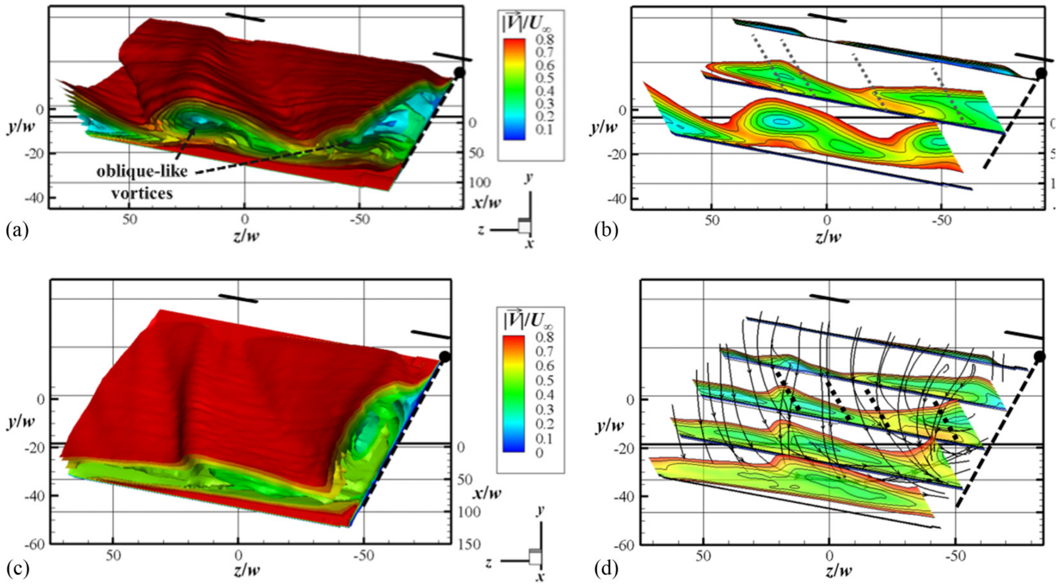


FIG. 12. Time-averaged flow field with every other jet active at the (a), (b) outboard and (c), (d) inboard zoomed-out locations. (a), (c) Isosurfaces of normalized total velocity, and normalized total velocity contours superimposed with 3D streamlines at (b) $x_{hl}/w = 13$, 44, and 75 for the outboard location and (d) $x_{hl}/w = 17$, 37, 57, 77, and 97 for the inboard location.

perpendicular to the control surface [Figs. 12(b) and 12(d)]. In the outboard region [Figs. 12(a) and 12(b)], the data show the presence of ridges (a velocity deficit with respect to the baseline) and recesses (velocity enhancement) in the $|\vec{V}|\ /U_\infty$ isosurfaces and contours, which are created by the jets. The recess in the center of the measurement domain is created by jet 5, and the effects of jets 3 and 7 are distinguishable at the outboard and inboard extremities of the measurement domain, respectively. The depth and spanwise extent of these features differs from the single jet case, showing that the jets affect each other even though they are far apart (the average spanwise spacing is 105% of the mean control surface chord). Moreover, the 3D streamlines, not presented for brevity, show a vortex inboard of jet 5's trajectory. This is believed to be an oblique-like vortex generated by the inboard jet (jet 7), similar, but not identical, to the vortex that was generated by a single jet and discussed in Jansen *et al.* [32].

The effect of every other jet activated at the inboard region is, unsurprising, quite different than at the outboard location. The height of the ridge and the corresponding velocity deficit, created by jet 9, are smaller because of the milder baseline separation. Also, at the outboard edge of the measurement domain, there is a ridge near jet 7, which is quite larger than the one associated with jet 9. The streamlines show evidence of a vortex in the jet 7 region, whereas there is no distinguishable one inboard of jet 9.

Next, all twelve jets are activated, as shown in Fig. 13. The effect of the jets on the outboard region is shown in Figs. 13(a) and 13(b), while the effect on the inboard region is presented in Figs. 13(c) and 13(d). In general, in the outboard region, activation of all the jets results in reducing the flow separation. There is a large variation in the effect created by adjacent jets along the span. The ridge and recess generated by jet 4 are larger in comparison to those related to the other jets. This can most likely be attributed to the larger spanwise spacing between jets 3 and 4 compared to the spacing of jets 4, 5, and 6. Moreover, streamlines (not given for brevity) show vortices in the isosurface regions, which are also believed to primarily be from an adjacent, inboard jet. Again, these are believed to be oblique-like vortices, which differ from the oblique vortex generated from

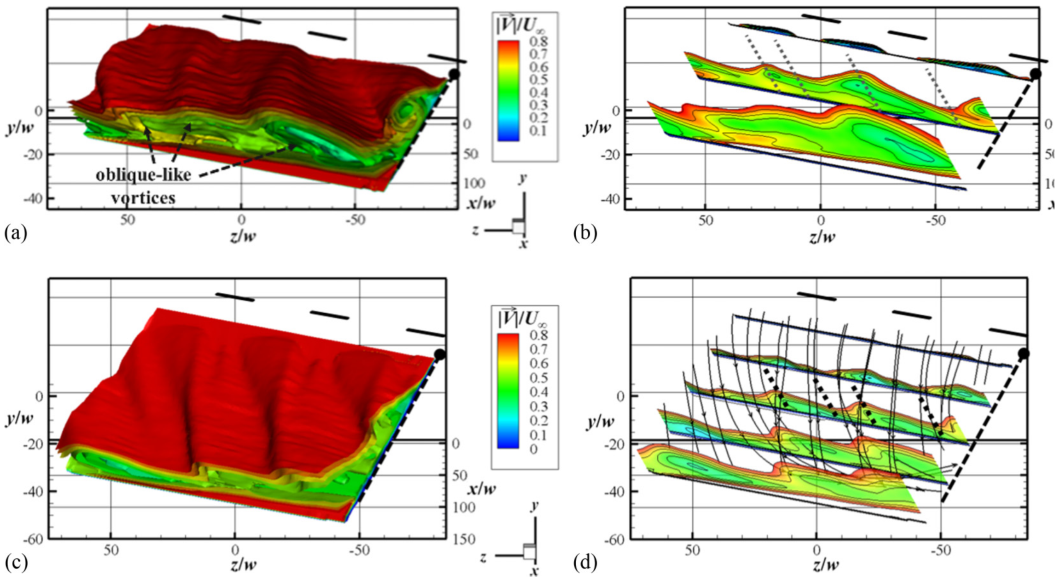


FIG. 13. Time-averaged flow field with all jets active at $C_b = 0.85$ and at the (a), (b) outboard and (c), (d) inboard zoomed-out locations. (a), (c) Isosurfaces of normalized total velocity and normalized total velocity contours superimposed with 3D streamlines at (b) $x_{hl}/w = 13$, 44, and 75 for the outboard location and (d) $x_{hl}/w = 17$, 37, 57, 77, and 97 for the inboard location.

a single jet (Jansen *et al.* [32]) due to the proximity of adjacent jets. This is discussed in more detail below.

In the inboard region, when all jets are activated, separation is reduced over nearly the entire measurement domain [Figs. 13(c) and 13(d)]. Once again, it is closer to being attached than at the outboard domain. However, there are still ridges and recesses in the isosurfaces associated with the jets' interaction with the crossflow. Furthermore, in general, the streamlines are turned downstream, and at many locations they are nearly parallel to the freestream.

In addition to the effect of all of the jets on the velocity field, their effect on the TKE field was also explored and is shown in Fig. 14. In the outboard region [Figs. 14(a) and 14(b)], each of the three jets whose trajectories intersect the plane at $x_{hl}/w = 13$ yield an increase in the TKE. Farther downstream, the TKE is increased relative to the baseline over the entire measurement domain, which is due to the unsteady nature of the synthetic jets. Moreover, as expected, the milder separation with all jet active at the inboard domain plays a role in the magnitude of the TKE at this location [Figs. 14(c) and 14(d)]. At the downstream planes ($x_{hl}/w = 57$, 77, and 97), the maximum TKE is smaller with all jets active relative to the other cases (baseline, single jet, every other jet). In addition, TKE is much larger at the outboard measurement domain than it is in this region. This is due to the fact that in the outboard region the effect of the jets in reducing the severity of separation is smaller than in the inboard region.

The interaction of multiple configurations of synthetic jets has primarily been qualitatively studied thus far. In order to quantitatively demonstrate their effect, profiles of time-averaged normalized velocity are shown next in the hinge-line axes. In the global wind axes, the velocity profiles do not show reversed flow over the control surface, because of the magnitude of the spanwise velocity component, and the adverse pressure gradient that essentially acts normal to the hinge-line (Wygnanski *et al.* [38]). Contrarily, velocity profiles in the hinge-line axes do show reversed flow and are therefore the more appropriate orientation of discussing separation using velocity profiles.

The velocity component perpendicular to the hinge-line and parallel to the control surface, $U_{hl}/U_\infty$, is presented for the outboard region at $x_{hl}/w = 44$ and $z_{hl}/w = -103$, $-63$, $-24$, and

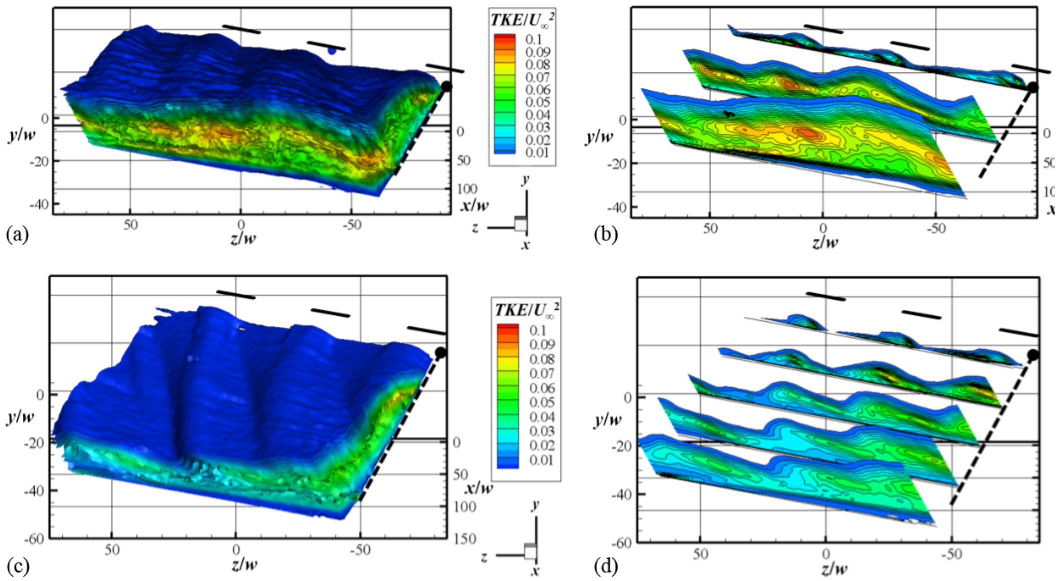


FIG. 14. (a), (c) Isosurfaces of $TKE/U_\infty^2$ with all synthetic jets active at $C_b = 0.85$ at the outboard and inboard regions, respectively. (b), (d) $TKE/U_\infty^2$ contours at $x_{hl}/w = 13, 44, 75$, and $x_{hl}/w = 17, 37, 57, 77, 97$ at the outboard and inboard locations, respectively.

$-10$ in Figs. 15(a)–15(d), respectively. As noted earlier, without actuation, the flow is separated over the control surface, the severity of which is approximately the same across the measured spanwise domain (i.e., the velocity deficit is roughly the same at different spanwise locations). The location farthest outboard, $z_{hl}/w = -103$ [Fig. 15(a)], corresponds to a recess in the isosurfaces of

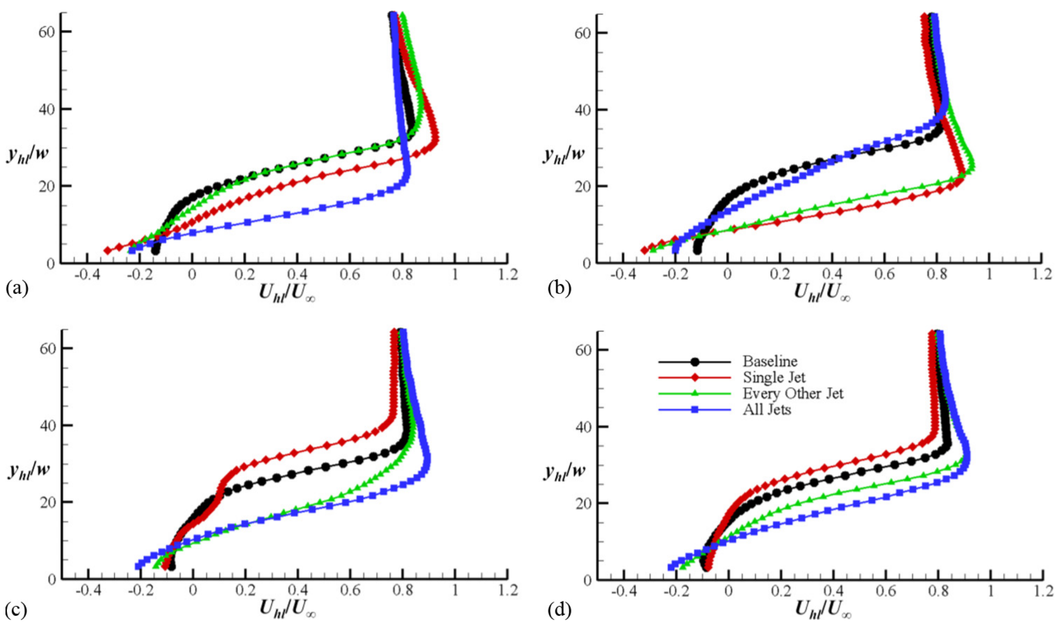


FIG. 15. Velocity profiles of time averaged $U_{hl}/U_\infty$ acquired at the outboard measurement domain, $C_b = 0.85$, $x_{hl}/w = 44$, and at $z_{hl}/w =$ (a) $-103$, (b) $-63$, (c) $-24$, and (d) $-10$.

total velocity for the case when all jets are on, where the velocity deficit is considerably reduced. However, the magnitude of the reversed flow near the wall is larger. This location also corresponds to where separation is approaching the baseline severity when a single jet is active. In this case, the shear layer is pulled slightly closer to the surface, and the velocity of the reversed flow near the wall increases. This is caused by the oblique vortex whose axis is between the streamwise and hinge-line directions, and consequently its velocity near the surface is partially oriented upstream. Furthermore, the effect of having every other jet active at this spanwise location is even less significant than when a single jet is on. The velocity profile is very similar to the baseline case; the only notable difference is enlarged flow reversal.

Figure 15(b) shows velocity profiles at $z_{\mathrm{hl}}/w = -63$, which corresponds to the spanwise location where a ridge is present when all the jets are actuated, as well as the location of a recess in the velocity contours when only jet 5 or every other jet are active. In the latter cases, the velocity deficit decreases, as expected, and the magnitude of the flow reversal near the surface increases. However, the velocity profiles of the baseline case and the case with all of the jets activated are very similar, with the largest difference being the stronger flow reversal in the actuated flow field.

At the spanwise location where a recess is present when all jets are active and where there is a ridge when only jet 5 is on [$z_{\mathrm{hl}}/w = -24$, Fig. 15(c)], the velocity deficit is larger with all jets active in this recess than it is farther outboard (at $z_{\mathrm{hl}}/w = -103$), once again demonstrating the complexity of the flow field when all jets are actuated. Additionally, even though there is a ridge near this location when every other jet is active, the profile is similar to the all-jets case near the surface (for $y_{\mathrm{hl}}/w \leqslant 20$), and every other jet has a much more favorable effect in comparison to when just jet 5 is on (in the vicinity of isosurface ridges). This is additional evidence that adjacent jets have a considerable influence on one another even with a large spanwise spacing, which is partially due to the large spanwise velocity from the swept and tapered configuration of the model.

The velocity profiles farthest inboard, $z_{\mathrm{hl}}/w = -10$ [Fig. 15(d)], correspond to the spanwise location of a ridge with all jets active. In this case, the jets reduce the velocity deficit. That is, the effect of the jets at this spanwise location is more favorable for separation control in comparison to the ridge outboard (at $z_{\mathrm{hl}}/w = -63$). With a single jet on, this profile is inboard of the virtual wall, and therefore is similar to the baseline case, both near the surface and at the edge of the shear layer.

In general, the flow fields corresponding to the different jet configurations in the outboard region are very complex. Therefore, it is important to a highlight a few key results. The flow is separated over the entire spanwise domain, the severity and features of which depend significantly on the case and spanwise location. The jets can deflect the shear layer toward the surface and reduce the thickness of the separated flow. Concurrently, the magnitude of the flow reversal near the wall is enhanced outboard of the jet structures for the single jet case and over the entire domain for the other actuated cases, which is related to the oblique vortex. Also, actuation with all jets is, overall, the most capable configuration that was tested for reducing flow separation. This is consistent with load measurements acquired in our applied work, presented in Table I and discussed in greater detail in Rathay *et al.* [36]. However, this case also requires the most power and therefore may not be the most efficient.

The qualitative effect of the synthetic jets on the flow field is relatively simpler in the inboard region. Figures 16(a)–16(d) show the velocity profiles at $x_{\mathrm{hl}}/w = 57$ (at 55% of the local control surface chord) and $z_{\mathrm{hl}}/w = -96$, $-64$, $-46$, and $-21$, respectively. Without actuation, the flow is separated, the extent of which increases in the outboard direction. The distance of the shear layer edge from the surface, the velocity deficit, and the magnitude of the reversed flow all become larger.

The location farthest outboard [$z_{\mathrm{hl}}/w = -96$, Fig. 16(a)] corresponds to a recess in the isosurfaces of total velocity (created by jet 8) with all jets active. The flow is almost completely attached; there is a small region of flow reversal near the wall ($y_{\mathrm{hl}}/w \leqslant 5$) in this case. With a single jet on, $z_{\mathrm{hl}}/w = -96$ is outboard of the recess. Nevertheless, activating a single jet still pulls the edge of the separated shear layer closer to the surface. Then, with every other jet active, the profile is very similar to the baseline case because $z_{\mathrm{hl}}/w = -96$ is near the large ridge inboard of jet 7.

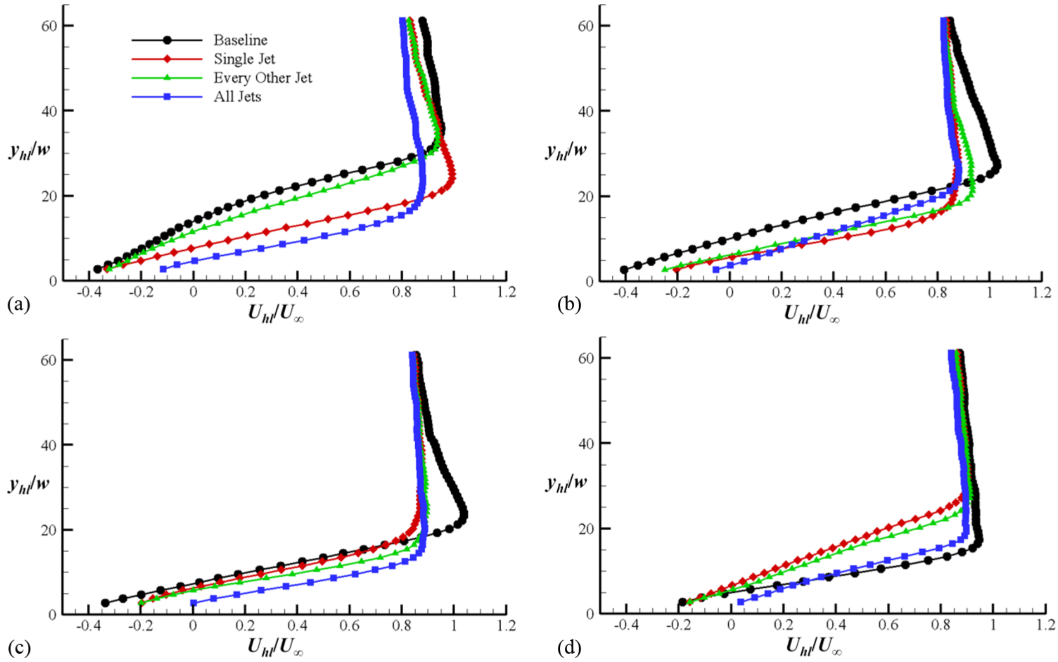


FIG. 16. Velocity profiles of time averaged $U_{\mathrm{hl}}/U_\infty$ acquired at the inboard measurement domain, $C_b = 0.85$, $x_{\mathrm{hl}}/w = 57$, and at $z_{\mathrm{hl}}/w =$ (a) $-96$, (b) $-64$, (c) $-46$, and (d) $-21$.

The spanwise location where $z_{\mathrm{hl}}/w = -64$ [Fig. 16(b)] relates to a ridge in the case when all jets are active, and a local minimum in the velocity contours with only jet 9 active. With just a single jet on, the distance of the shear layer from the surface is reduced. On other hand, this distance does not change much with the activation of all jets. However, the region of flow reversal decreases by a substantial amount, more than that achieved with only a single jet active.

At $z_{\mathrm{hl}}/w = -46$ [Fig. 16(c)], which corresponds to a valley in the flow field (from jet 9) when all jets and every other are activated, the flow seems to be completely reattached with the activation of all jets. The same is true at $z_{\mathrm{hl}}/w = -21$ [Fig. 16(d)], which is actually at a ridge for all of the cases in which the jets are on. This shows that near the trajectory of jet 9 this synthetic-jet-based flow control configuration is relatively effective.

Overall, at the inboard region, reducing the velocity deficit does not correspond to enhanced flow reversal near the wall. The opposite was observed outboard, most likely because there were no oblique vortices observed at the inboard location. In addition, the data further show that the jets were more capable of controlling the milder separation inboard, and the most effective case was when all of the jets were active.

To further analyze the interaction of different combinations of jets, the time-averaged streamwise vorticity field is presented at both locations when every other jet [Figs. 17(a) and 17(c)] and when all jets are active [Figs. 17(b) and 17(d)]. Only time-averaged data are presented for brevity.

At the outboard region, when all the jets are actuated, the negative concentration of vorticity associated with jet 6 can be seen at the inboard (left) portion of the measurement domain [Fig. 17(b)]. The trajectories of jets 5 and 4 are completely captured in the flow volume, and jet 3 is near the outboard side of the figure. This concentration and the one related to jet 5 are also captured when every other jet is active [Fig. 17(a)]. The structures generated when every other and all jets are active interact with the crossflow differently than those created when a single jet is active. For one, the negative concentrations of $\Omega_x$ maintain their initially trajectory more when an array of actuators is active. Specifically, the angle between jet 5's negative concentration and the streamwise,

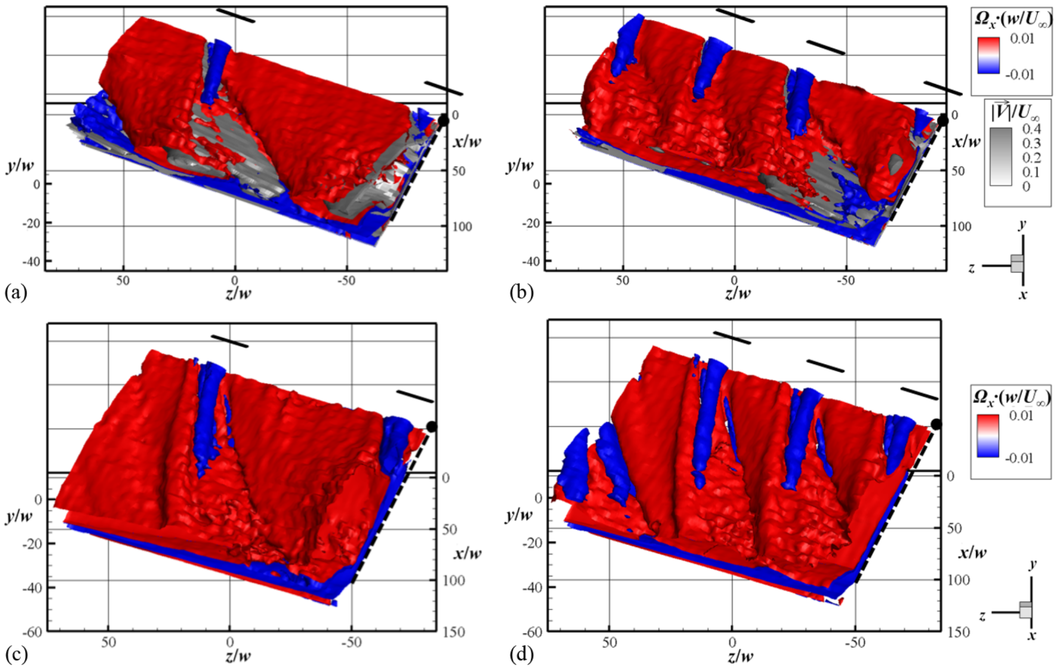

FIG. 17. Isosurfaces of normalized streamwise vorticity at the (a), (b) outboard and (c), (d) inboard zoomed-out regions. Time-averaged data with (a), (c) every other jet and (b), (d) all jets active.

$x$, direction over the control surface is roughly 13°, 6°, and 0° with all, every other, and one jet active, respectively. Moreover, negative $\Omega_x$ dissipates quicker when more jets are activated. The negative concentration from a single jet is larger than with arrays of jets, and with every other jet active, the negative concentration persists slightly farther downstream than with all jets. This shows that the strength of the vortical structures (represented by negative $\Omega_x$ here) is reduced because of the interaction between adjacent jets. This is believed to be partially related to their interaction with adjacent oblique vortices, which generate positive $\Omega_x$.

These data demonstrate the trade-offs associated with changing the spanwise spacing of actuators at the outboard location. In one respect, denser placement of jets means that a larger number can be used for flow control. This equates to larger $C_\mu$, which is well known to be an important parameter for separation control. On the contrary, when the spanwise spacing between jets is decreased at this location, adjacent jets affect each other in such a way that the strength of the jets' vortical structures reduces. In addition, larger jet spacing is believed to allow for greater growth of oblique vortices, which, as discussed in Jansen *et al.* [32], can generate lift. With the configuration tested here, when the density of actuators increases, the larger $C_\mu$ outweighs the weaker jet and oblique vortices. In some of our other applied work though, different trends were measured (Rathay *et al.* [30]); reducing spacing (with a constant $C_b$) resulted in greater lift augmentation. In this case, the jet spacing was the same and control surface chord was twice the size of the one presented here. Therefore, the total $C_\mu$ was approximately half of the larger model. This indicates that when $C_\mu$ is limited, increasing jet spacing to augment the strength of oblique vortices may be an effective control strategy in flows with a strong spanwise component.

As expected, the streamwise vorticity field is different at the inboard measurement domain. The negative vorticity concentration associated with jet 9 (black line farthest inboard) persists farther downstream when all jets are active [Fig. 17(d)] in comparison to the case with every other jet active [Fig. 17(c)]. Additionally, the negative vorticity concentrations associated with jet 9 in the latter case appear quite similar to when a single jet is on [Fig. 5(b)]; the streamwise vorticity is visible slightly

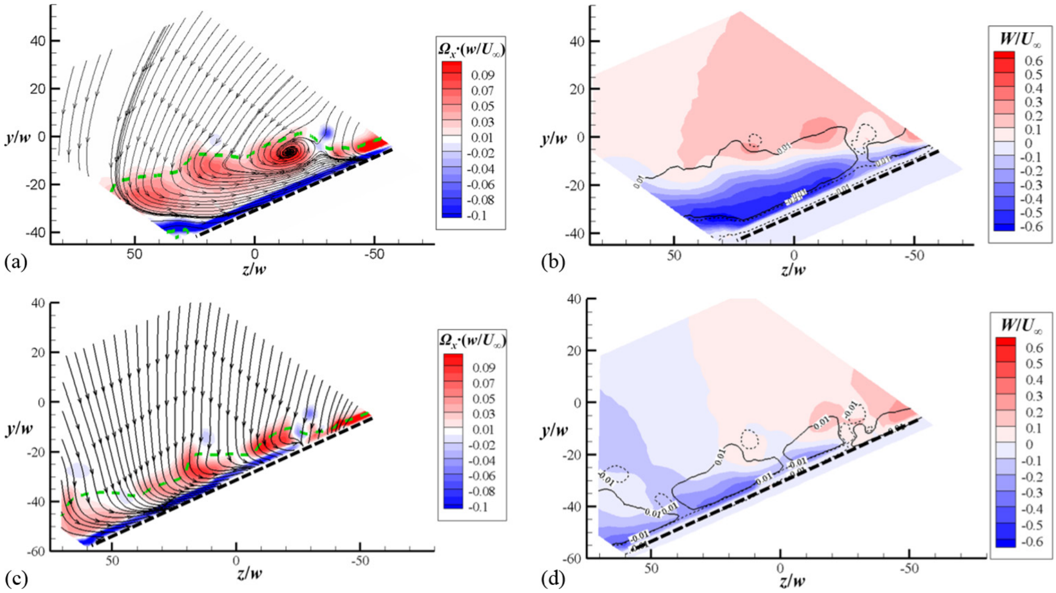

FIG. 18. Time-averaged flow field with all jets active presented in planes perpendicular to the streamwise direction at $x/w = 56$ for the (a), (b) outboard and (c), (d) inboard regions. (a), (c) Color contours of normalized streamwise vorticity superimposed with in plane streamlines and a green contour line corresponding to $|\vec{V}|/U_\infty = 0.7$, and (b), (d) color contours of normalized spanwise velocity superimposed with line contours of normalized streamwise vorticity.

farther downstream with every other jet active. Furthermore, jet 8 appears to dissipate more quickly than jet 9 when all jets are on. This is presumably related to the extent of the flow separation in the baseline case, which grows in the outboard direction.

These results show that in the inboard region and for the conditions tested, reducing the spanwise spacing between active jets reduces the rate at which their structures dissipation (i.e., they favorably affect each other). In the outboard region on the other hand, the opposite trend was seen. (Note that the control surface on the tapered model is roughly 30% larger at the inboard location, which can make the figures misleading). This difference is, for one, believed to be related to the absence of distinguishable oblique vortices inboard. Also, a jet within an array of active jets is believed to benefit from the greater reduction in separation created by adjacent actuators at the inboard location. Furthermore, the variance in the strength of the jets' vortical structures between configurations when a single and every other actuator is on is much smaller in the inboard region than in the outboard. This suggests (as did the $U_{\mathrm{hl}}/U_\infty$ velocity profiles) that in the inboard, less separated region, the spacing when every other jet is activated is such that the jets do not have a significant effect on one another in comparison to the corresponding case in the outboard region.

To further analyze why the jets' vortical structures decrease in strength as the spanwise spacing among jets is reduced at the outboard region, time-averaged data are presented in Fig. 18(a) when all jets are active. Here, normalized $\Omega_x$ is given at $x/w = 56$. The negative concentration of $\Omega_x$ from jet 5 is located around $z/w = 17$ and $y/w = -20$, and as discussed above, it is weaker relative to the case when just a single jet is on. Additionally, in this plane, there is no evidence of a vortex inboard of the virtual wall from jet 5; however, it is visible in planes farther upstream that are not given for brevity. There is a large vortex at this streamwise location outboard of jet 4 though, partially because the jet orifice is closer to this plane ($x/w = 56$). Moreover, one of the most notable differences with all jets in comparison to other cases is the much larger positive $\Omega_x$ concentrations here.

The effect of all the jets on the spanwise velocity at the outboard location is given in Fig. 18(b). The jets increase the spanwise velocity near the control surface over nearly the entire measurement domain (to more than 60% of the freestream velocity in some places). This supports the qualitative trends observed with tuft flow visualizations in our previous work (Rathay *et al.* [36]), where the flow turned outboard in this region when all of the jets were actuated. Recall that the spanwise velocity magnitude was only enhanced outboard, not inboard, with only one jet on, because of the oblique vortex. This further supports the hypothesis that that the augmentation of $W$ in the vicinity of a particular jet is likely created by the oblique vortex inboard of it. Moreover, this figure shows that the positive concentrations of $\Omega_x$ are associated with the large gradient of $W$ in the $y$ direction.

The streamwise vorticity field at the inboard location exhibits negative vorticity concentrations, which are related to jets 8, 9, and 10 (in the positive $z$ direction) with all jets active [Fig. 18(c)] and are stronger than the same features observed outboard. In addition, there are ridges in the positive $\Omega_x$ contours that correspond to peaks in the total velocity contour line at the inboard region, akin to those observed in other cases. Overall, the positive $\Omega_x$ (associated with the crossflow) is reduced relative to the baseline case and the corresponding case at the outboard location. Last, spanwise velocity is presented at the inboard location [Fig. 18(d)]. The maximum spanwise velocity at $x/w = 56$ decreases from 63% in the baseline to approximately 41% with all jets active, given that there are no visible oblique vortices. This was also qualitatively observed with tuft flow visualizations in our previous work (Rathay *et al.* [36]), which showed that at this spanwise location the tufts turned toward the freestream direction with all jets active.

In summary, the data collected at the outboard region suggest that the jets' structures dissipate more quickly as the proximity of adjacent active jets increases, because of oblique vortices that are compressed and have a greater effect as more jets are actuated. However, these structures are not visible at the inboard region, presumably since the jets are more effective at reducing separation, and the vortical structures associated with jet 9 dissipate more gradually as the number of jets increases. This lends insight into future methods of more effectively controlling separation with variable severity. Contrary to initial predictions, if restricted by total $C_\mu$ (at these levels), a larger quantity of jets should actually be placed in regions where they are more capable of reducing separation (i.e., inboard), and the spacing between jets should be increased at locations in which separation is more severe, where they can create oblique vortices (i.e., outboard).

## IV. CONCLUSIONS

An array of twelve synthetic jet actuators were installed upstream of the control surface hinge-line on a swept and tapered wind tunnel model. The control surface was deflected at an angle of 30°. Three configurations of jets were tested, including all jets active, every other jet active and a single jet active. Their interaction with the crossflow at inboard and outboard locations on the model was captured using SPIV and analyzed in detail.

The data showed that the baseline flow field at the outboard location was characterized by a severely separated flow that originated at the hinge-line. The separation was quasiuniform in the spanwise direction and had a strong spanwise velocity component. At the inboard region, the baseline flow field was also separated, but the severity was much milder. Additionally, the separation severity increased in the spanwise direction, and in this region a large vortex was observed, whose axis of rotation was angled downstream and slightly outboard. It was argued that this vortex was created because of differences in separation severity and the spanwise crossflow. The vortex seemingly further augmented the negative spanwise velocity near the surface further in its vicinity.

Actuation with a single jet was first studied. At the outboard location, zoomed-in phase-averaged SPIV measurements were leveraged to describe how the jets vortical structures interacted with the separated crossflow. Furthermore, zoomed-out measurements at the inboard and outboard locations showed that the severity of flow separation was reduced at both locations. However, due to differences in baseline separation severity, when the synthetic jet was activated the flow was closer to being attached inboard. In the outboard measurement domain, there was a vortex outboard of the jet structures where separation severity was approaching the baseline state. This oblique vortex was very similar to the one observed inboard in the baseline flow field. As noted in our previous work, the oblique vortex was a very important feature with respect to lift augmentation on the wing.

In general, the separation severity decreased as more jets were activated. However, the complexity of the flow field grew as well, most notably at the outboard location. In this region, the strength of the vorticity concentrations, associated with the jets, decreased as more jets were activated, whereas the opposite trend was observed at the inboard region. In addition, when the jets were activated, the spanwise velocity magnitude increased and decreased at the outboard and inboard locations, respectively. These observations were believed to be related to the oblique vortices in the outboard region, the effects of which presumably grew as more jets were activated and the distance from the jet structures to the oblique vortices was reduced. Moreover, based on these results, it was argued that for a configuration where separation severity is varying, a larger quantity of jets should be placed in regions where they are more capable of reducing separation (i.e., inboard), and the spacing between jets should be increased at locations in which separation is severe and they form oblique vortices (i.e., outboard). From a designer point of view, the information in the paper that can help in the design of a more efficient flow control system is the fact that spacing between jets is important, especially in the presence of a massive flow separation and a large spanwise velocity, where there can be a destructive interaction between jets. Clearly, a more detailed sensitivity analysis is needed, which is out of the scope of this paper.

## ACKNOWLEDGMENTS

The authors thank Michel Rasquin and Kenneth Jansen from the University of Colorado at Boulder. The knowledge gained from their simulations was very important in enhancing our understanding of the interaction of synthetic jets in this complex flow field. The authors also thank the Boeing Company for support.

---

[1] S. G. Anders, W. L. Sellers III, and A. E. Washburn, Active flow control activities at NASA Langley, AIAA Paper No. 2004-2623 (2004).

[2] L. N. Cattafesta III and M. Sheplak, Actuators for active flow control, Ann. Rev. Fluid Mech. **43**, 247 (2011).

[3] B. L. Smith and A. Glezer, The formation and evolution of synthetic jets, Phys. Fluids **10**, 2281 (1998).

[4] A. Glezer and M. Amitay, Synthetic Jets, Ann. Rev. Fluid Mech. **34**, 503 (2002).

[5] B. L. Smith and G. W. Swift, A comparison between synthetic jets and continuous jets, Exp. Fluids **34**, 467 (2003).

[6] T. Van Buren and M. Amitay, Comparison between finite-span steady and synthetic jets issued into a quiescent fluid, Exp. Therm Fluid Sci. **75**, 16 (2016).

[7] M. Amitay and F. Cannelle, Evolution of finite span synthetic jets, Phys. Fluids **18**, 054101 (2006).

[8] C. Yao, F. J. Chen, and D. Neuhart, Synthetic jet flowfield database for computational fluid dynamics validation, AIAA J. **44**, 3153 (2006).

[9] R. B. Kotapati, R. Mittal, and L. N. Cattafesta III, Numerical study of a transitional synthetic jet in quiescent external flow, J. Fluid Mech. **581**, 287 (2007).

[10] T. Van Buren, E. Whalen, and M Amitay, Vortex formation of a finite-span synthetic jet: High Reynolds numbers, Phys. Fluids **26**, 014101 (2014).

[11] T. Van Buren, E. Whalen, and M. Amitay, Vortex formation of a finite span synthetic jet: Effect of rectangular orifice geometry, J. Fluid Mech. **745**, 180 (2014).

[12] A. Crook and N. Wood, Measurements and visualizations of synthetic jets, AIAA Paper No. 2001-0145 (2001).

[13] S. Zhong, M. Jabbal, H. Tang, L. Garcillan, F. Guo, N. Wood, and C. Warsop, Towards the design of synthetic-jet actuators for full-scale flight conditions, Flow Turbul. Combust. **78**, 283 (2007).

[14] D. K. Wu and M. A. Leschziner, Large-eddy simulations of circular synthetic jets in quiescent surroundings and in a turbulent cross-flow, Int. J. Heat Fluid Flow **30**, 421 (2009).
[15] R. Mittal, P. Rampunggoon, and H. S. Udaykumar, Interaction of a synthetic jet with a flat plate boundary layer, AIAA Paper No. 2001-2773 (2001).
[16] T. Van Buren, C. Leong, M. Beyar, and M. Amitay, Three-dimensional interaction of a finite-span synthetic jet in a crossflow, Phys. Fluids **28**, 037105 (2016).
[17] D. R. Smith, Interaction of a synthetic jet with a crossflow boundary layer, AIAA J. **40**, 2277 (2002).
[18] M. Watson, A. J. Jaworski, and N. J. Wood, Contribution to the understanding of flow interactions between multiple synthetic jets, AIAA J. **41**, 747 (2003).
[19] M. A. Leschziner and S. Lardeau, Simulation of slot and round synthetic jets in the context of boundary-layer separation control, Philos. Trans. R. Soc. A: Math. Phys. Eng. Sci. **369**, 1495 (2011).
[20] D. C. McCormick, Boundary layer separation control with directed synthetic jets, AIAA Paper No. 2000-0519 (2000).
[21] M. Amitay and A. Glezer, Role of actuation frequency in controlled flow reattachment over a stalled airfoil, AIAA J. **40**, 209 (2002).
[22] M. Amitay, D. R. Smith, V. Kibens, D. E. Parekh, and A. Glezer, Aerodynamic flow control over an unconventional airfoil using synthetic jet actuators, AIAA J. **39**, 361 (2001).
[23] M. DeSalvo, E. Whalen, and A. Glezer, High-lift enhancement using active flow control, AIAA paper 2012 (2012).
[24] D. Greenblatt and A. E. Washburn, Influence of finite span and sweep on active flow control efficacy, AIAA J. **46**, 1675 (2008).
[25] T. Holl, E. Wassen, and F. Thiele, Active separation control on a high-lift configuration using segmented actuation slots, AIAA paper No. 2010-4249 (2010).
[26] O. Sahni, J. Wood, K. E. Jansen, and M. Amitay, Three-dimensional interactions between a finite-span synthetic jet and a crossflow, J. Fluid Mech. **671**, 254 (2010).
[27] Y. Elimelech, J. D. Vasile, and M. Amitay, Secondary flow structures due to interaction between a finite-span synthetic jet and a 3D cross flow, Phys. Fluids **23**, 094104 (2011).
[28] J. D. Vasile and M. Amitay, Interactions of an array of finite span synthetic jets and a crossflow, AIAA J. **51**, 2503 (2013).
[29] B. H. Maines, B. R. Smith, D. Merrill, S. Saddoughi, and H. Gonzalez, Synthetic jet flow separation control for thin wing fighter aircraft, AIAA Paper No. 2009-885 (2009).
[30] N. Rathay, M. Boucher, M. Amitay, and E. Whalen, Application of synthetic jets to enhance the performance of a vertical tail, SAE Int. J. Aerospace **6**, 169 (2013).
[31] N. Rathay, M. Boucher, M. Amitay, and E. Whalen, Performance enhancement of a vertical tail using synthetic jet actuators, AIAA J. **52**, 810 (2014).
[32] K. E. Jansen, M. Rasquin, J. A. Farnsworth, N. Rathay, M. C. Monastero, and M. Amitay, Interaction of a synthetic jet with separated flow over a vertical tail, AIAA J. **56**, 2653 (2018).
[33] T. J. Mueller and M. B. Stephen, Experimental studies of separation on a two-dimensional airfoil at low Reynolds numbers, AIAA J. **20**, 457 (1982).
[34] A. K. Prasad, Stereoscopic particle image velocimetry, Exp. Fluids **29**, 103 (2000).
[35] N. Rathay, M. Boucher, M. Amitay, and E. Whalen, Parametric study of synthetic-jet-based flow control for performance enhancement of a vertical tail, AIAA J. **52**, 2440 (2014).
[36] D. I. Poll, Spiral vortex flow over a swept-back wing, Aeronaut. J. **90**, 185 (1986).
[37] F. F. Grinstein, Vortex dynamics and entrainment in rectangular free jets, J. Fluid Mech. **437**, 69 (2001).
[38] I. Wygnanski, P. Tewes, and L. Taubert, Applying the boundary-layer independence principle to turbulent flows, J. Aircraft **51**, 175 (2014).